ISSN 0972-5741 Volume 128, Issue 2, April 2021

IGC Newsletter

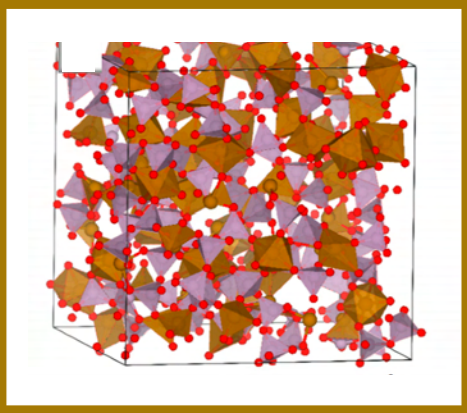

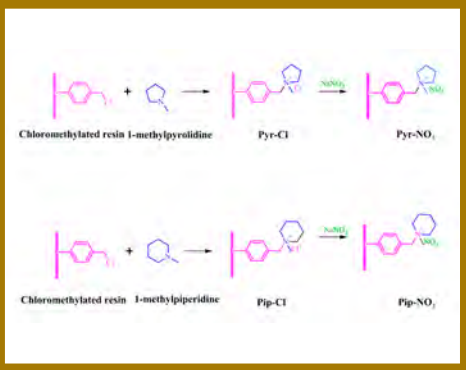

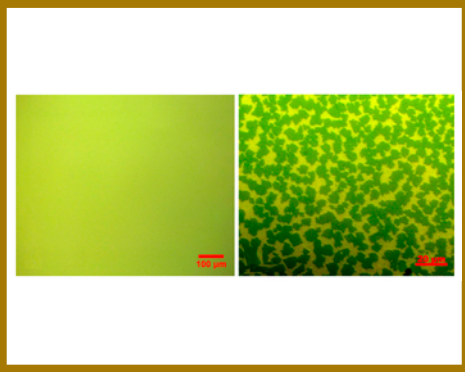

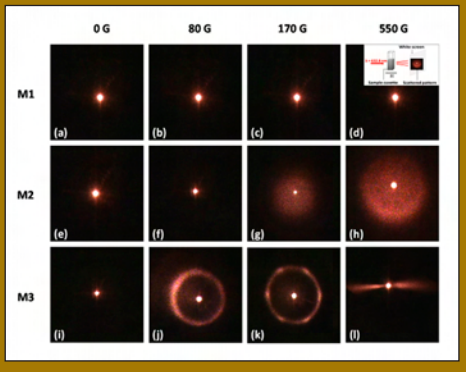

INDIRA GANDHI CENTRE FOR ATOMIC RESEARCH
http://www.igcar.gov.in/lis/nl128/igc128.pdf

From the Editor's Desk

Dear Reader

It is my pleasant privilege to forward the latest issue of IGC Newsletter (Volume 128, April 2021, Issue 2). I thank my team for their timely inputs, cooperation, and support in bringing out this issue.

The digital copy is published through the websites http://vaigai and http://www.igcar.gov.in. Additionally, on the Vaigai website, the flip copy of the Newsletter is available.

The technical article is on"Developing Atomistic Glass Models using Potential-Free Monte-Carlo Method." The article is contributed by Shri Shakti Singh and his colleagues from the Materials Physics Division of Materials Science Group.

Young Officer's Forum features an article by Dr. Ch. Kishan Singh, Materials Science Group. Shri Dillip Kumar Mohapatra of Metallurgy & Materials Group, IGCAR, has contributed Young Researcher's Forum article on this issue.

Further, we have included highlights of our colleagues' awards, honors, and recognitions in this issue.

The back cover of the IGC Newsletter is adorned by Asian Paradise Flycatcher, which was first spotted by our photographer in the DAE complex, Kalpakkam, in June 2018 during its breeding season.

The Editorial Committee would like to thank all the contributors. We look forward to receiving constructive suggestions from readers towards improving the IGC Newsletter content.

Use Face Mask. Maintain Social Distance to break the chain. Vaccinate. Stay Safe.

With best wishes and regards

S. Rajeswari
Chairman, Editorial Committee, IGC Newsletter and
Head, Scientific Information Resource Division, IGCAR

Developing Atomistic Glass Models using Potential-Free Monte-Carlo Method

The endeavour to model atomistic structures of glasses or more generally amorphous materials has been around since the time X-ray diffraction technique gained recognition for uniquely determining the crystal structures. For amorphous systems, most experimental probes give reliable information only upto short-range (~3 Å) since the intermediate-range (~ 4-8 Å) and long-range information is averaged out in all the experimental probes due to randomness in structure at these length scales. This shortcoming of experiments to fully predict the atomistic structure of glass is a well-known fact and warrants the need of computational models to study glasses.

Atomistic structure of glass holds the key to microscopic explanation of a range of problems like reason for their stability, reason for superior Glass Forming Ability (GFA) of certain compositions of elements over the other, superior chemical durability of certain glass compositions over others, radiation cascade studies for suitability in vitrification of waste generated from reprocessing of spent nuclear fuel and development of interatomic potentials for Molecular Dynamics (MD) simulation of glasses. Due to the computational progress made in the last two decades, with the advent of fast cluster computing facilities and highly parallel codes of ab-initio calculations, it is now possible to develop atomistic models of any system by simulating the experimental melt-quench technique albeit at very fast time scale (picoseconds in Density Functional Theory (DFT) to nanoseconds in MD). The shortcoming of such simulation is that the cooling rates (CRs) employed are extremely fast (~10^{13} K/s) as compared to experimental CRs (typically 10 K/s for air quenching). Due to this the system is found to possess many characteristics of the starting structure which is melted and quenched. For correctly predicting a glass model, one ideally should start with perfectly random structure which is never the case. Most current studies start with a crystal structure that closely mimics the connections of constituent units found in glass. So the issue which the method presented here addresses is the requirement of correct starting structures in glass simulations. If starting structures are fairly glassy (in the sense that they obey most of the experimentally known short-range and medium-range properties of that glass at the same time lack long-range order) then the final structures could be more promising. Such starting structures can also expedite the geometry relaxation jobs in ab-initio MD based development of glasses or in Reverse Monte Carlo (RMC) methods. The fundamental reason why this should work can be seen from the potential energy landscape (PEL). By prebuilding the features known experimentally into the developed models it is ensured that the algorithm stays near the metastable glass valley in the PEL and hence convergence can not only be guaranteed but it will also be quick. Also, whereas going ab-initio in calculations is advisable yet due to high computational cost one cannot develop structure beyond hundreds of atoms. So one can do away with the requirement to go ab-initio right at the start. In the method presented here, an algorithm is developed based on Monte-Carlo

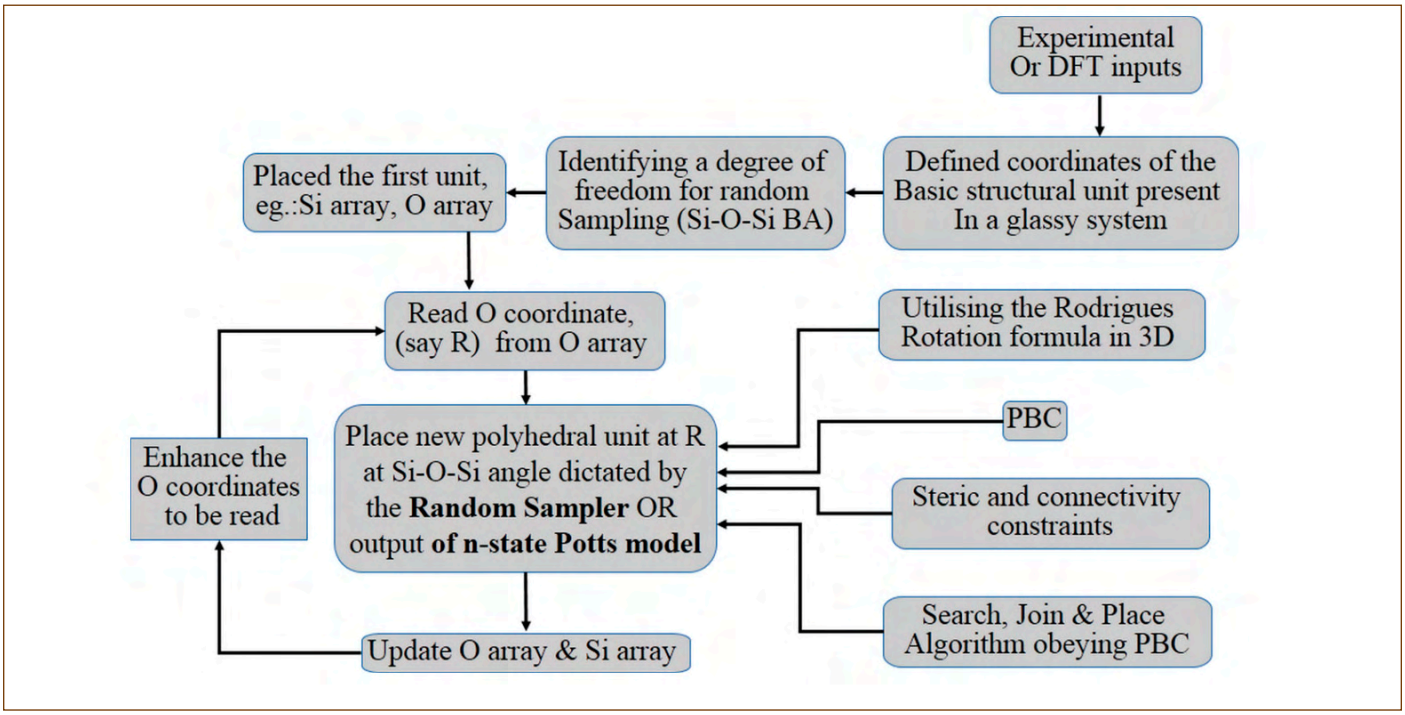

Figure 1: Flowchart of the MC algorithm used for developing glass structure

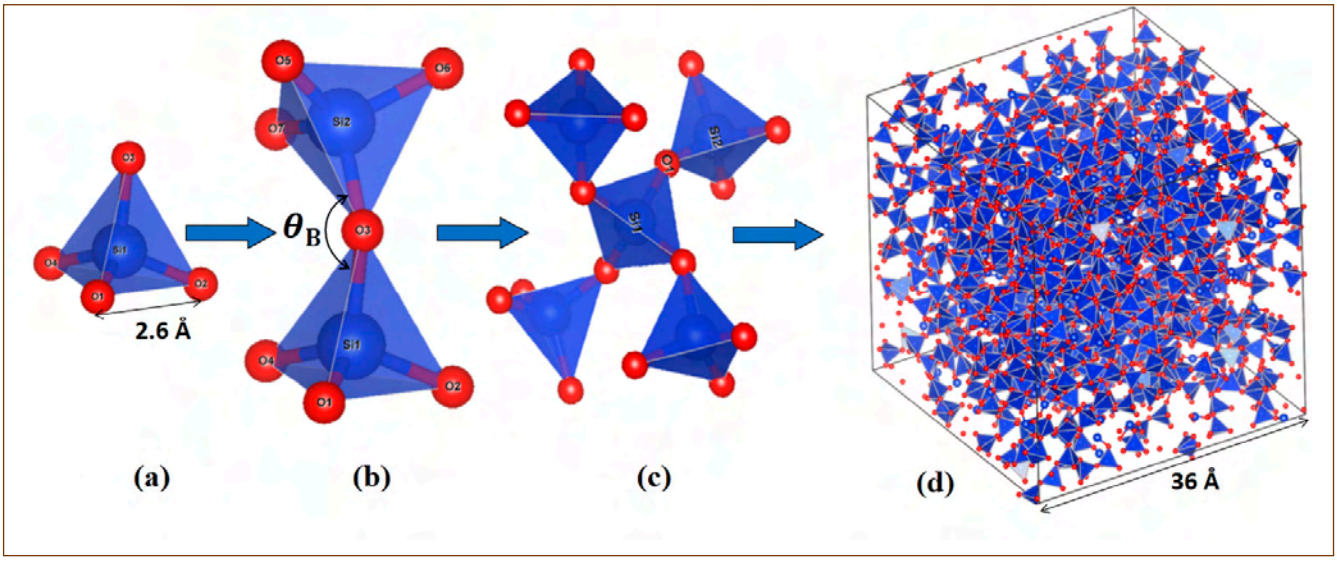

Figure 2: Successive stages involved in developing silica glass structure (a) the input tetrahedral unit (b) the dimer unit obtained by placing another tetrahedral unit at one of the corner oxygen atoms (c) all four oxygen atoms of central motif bridged (d) steps (a)-(c) repeated for all oxygen atoms to develop structure of silica glass consistent with PBC, having density of 2.10 g/cc

(MC) method that uses only short-range information to develop atomistic models of glasses.

Method overview

The intricacies involved in modelling any glass structure can be explained using silica as an example. It is well-known that silica glass structure consists of randomly connected tetrahedral units $[SiO_4]^{4-}$ having corner sharing oxygen. The algorithm used to develop this structure is shown in Figure 1. Starting with the short-range information available apriori for most glasses from X-ray and neutron diffraction experiments or ab-initio studies like DFT, one defines the coordinates of the smallest repeatable motif which for the case of SiO_2 is the $[SiO_4]^{4-}$ tetrahedral unit. Then from the well-established observation that disorder in glass structure can be attributed to the randomness involved in the way these motifs connect with each other, we identify an orientational degree of freedom (dof) of the structure which can be randomised to obtain a random-network. This is the basic motivation behind the application of random numbers and hence the MC method in modelling random glass structures. For the case of SiO_2, this dof is the Si-O-Si angle, also called inter-tetrahedral or bridging bond-angle. Experimentally, the distribution of this bond angle is found to be in range [120°, 180°] with a peak at 147°. Hence it is this dof of the structure that is sampled using random number generator with appropriate constraints to match the experimentally observed distribution of bond angle. Now a simulation box is defined and the first motif is placed at a random position inside it. Computationally, this amounts to assigning coordinate positions of oxygen and silicon atoms to an array. Now the oxygen coordinates are successively read from this array and new motifs are placed at each of the vertex oxygen at the Si-O-Si bond angle dictated by a Random Sampler. The array is updated each time a new unit is placed. We have also tried to use the output of n-state Potts model to sample the orientational dof in glass. The spin orientations in Potts model can be correlated to the orientation of polyhedral units in glasses. But due to the discreteness of spin orientations in Potts model, it was concluded that for modelling glasses it is more appropriate to use a continuous random sampler available in most programming languages. The code is programmed in Python, and hence its random sampler is used which is based on Mersenne-twister algorithm. The random rotation of tetrahedral unit about the Si-O axis is performed using the Rodrigues rotation formula. Only those units are placed which are permitted by the constraints. The search, join and place algorithm is necessary to reproduce the ring topology of the glassy structure. Lastly the Periodic Boundary Condition (PBC) is very important if the structure has to correctly reproduce the experimental density, stoichiometry and void distribution. Figure 2 shows the schematics of developing glassy structures of SiO_2 within a cubic simulation box of 36 Å by this method. The final structure developed is also shown in Figure 2(d). For visualization, VESTA software is used. Important constituents of the algorithm are explained next.

Constraints and 3D rotation

The motifs placed inside the simulation box must always adhere to the steric constraints between constituent atoms. For this purpose, successive motifs are placed so that all the atoms have these constraints satisfied. The minimum cut-offs for oxygen and silicon atoms belonging to different motifs are O_i-O_j = 2.3 Å,

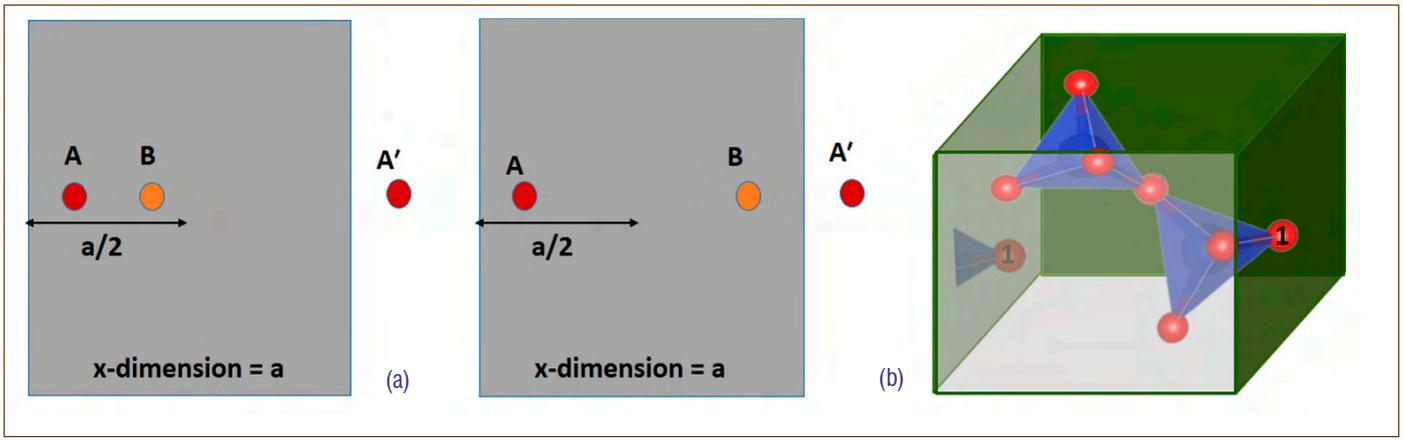

Figure 3: PBC (a) Distance calculation in periodic structures (b) Periodic wrapping of the tetrahedral unit from opposite wall

Si_i-Si_j = 2.7 Å where i and j subscripts belong to two different polyhedral motifs. Similarly, the bond-angle Si-O-Si is allowed to vary between 120˚ and 180˚ and rest of the values are prohibited. For 3D rotation of the motifs inside the simulation box, the Rodrigues Rotation formula is used to rotate a vector in space given an axis and an angle of rotation (θ). Axis for this purpose is taken to be in Si-O direction where O is the oxygen on which the next motif is planned.

Search, Join and Place algorithm

The motifs placed successively should also form closed ring like structure instead of forming a dendrite like structure. Such ring like structures are characteristic of the intermediate-range order found in most glasses and also hold the key for first sharp diffraction peak (FSDP) seen universally in structure factor of glasses. So an algorithm takes care of forming these rings by searching for nearby oxygen and utilising them as either edge or face of forthcoming motif being placed. Consistency of this algorithm with Periodic Boundary Condition is also ensured. It is named as the search, join and place algorithm after the steps that are involved in this algorithm.

Periodic Boundary Conditions (PBC)

Since the method is developed keeping in mind the application of generated models in ab-initio methods of analysis, the models should obey PBC. For ensuring this all the distances in the program are calculated respecting PBC i.e. if the difference between the x, y, z coordinates of atom A and atom B is less than or equal to half of the respective dimension of the cube along that axis, then the original distance AB is minimum distance between those points. But for the other case, where the difference exceeds half of cell dimension along that axis, atom A is translated by the cell dimension along that axis and distance A′B between image of atom A i.e. A′ and atom B is considered as the shortest distance. A pictorial aid for understanding this is given in Figure 3(a). Distance calculation is a central part of the program since all the atoms should follow the constraint cut-offs placed for ensuring that no two atoms come closer than a cut-off distance. Also, while generating the model, atom moving out from any boundary wall is wrapped inside from the opposite wall using the PBC equations. During such wrapping, the PBC image may end up getting too close to oxygen of tetrahedral unit already placed. This warrants the constraint cut-offs to be adhered in consistency with PBC. This is shown in Figure 3(b). Although periodicity in amorphous structures is not present, still for the purpose of modelling it becomes a necessary evil. The effect of periodicity on the predicted properties is also an area of study in amorphous modelling.

Structural analysis of the developed models

The presented algorithm is used to first develop silica glass model to validate it. Thereafter, Iron Phosphate Glass (IPG) models, which possess more complex geometry than typical binary glasses are also developed. For characterising these network glass models, following structural tools have been adopted at different length scales:

1. Short-range structure analysis: The short-range structure is decided predominantly by chemical bonding involved, it tells about the basic geometry in glasses which is repeated throughout in the 3-dimensional structure and also how it is connected to its neighbours. This information about glasses is readily available from experiments like Neutron Diffraction, Raman spectroscopy, EXAFS, NMR etc. So the structural properties of generated models at short length scales that can be compared with experiments are: Radial distribution function (RDF) for nearest neighbour and next nearest neighbour bond distances, structure factor S(Q), bond-angles, dihedral bond angle, coordination number analysis.

2. Intermediate-range structure analysis: This is decided mainly by the kinetics of glass formation. The difficulty of

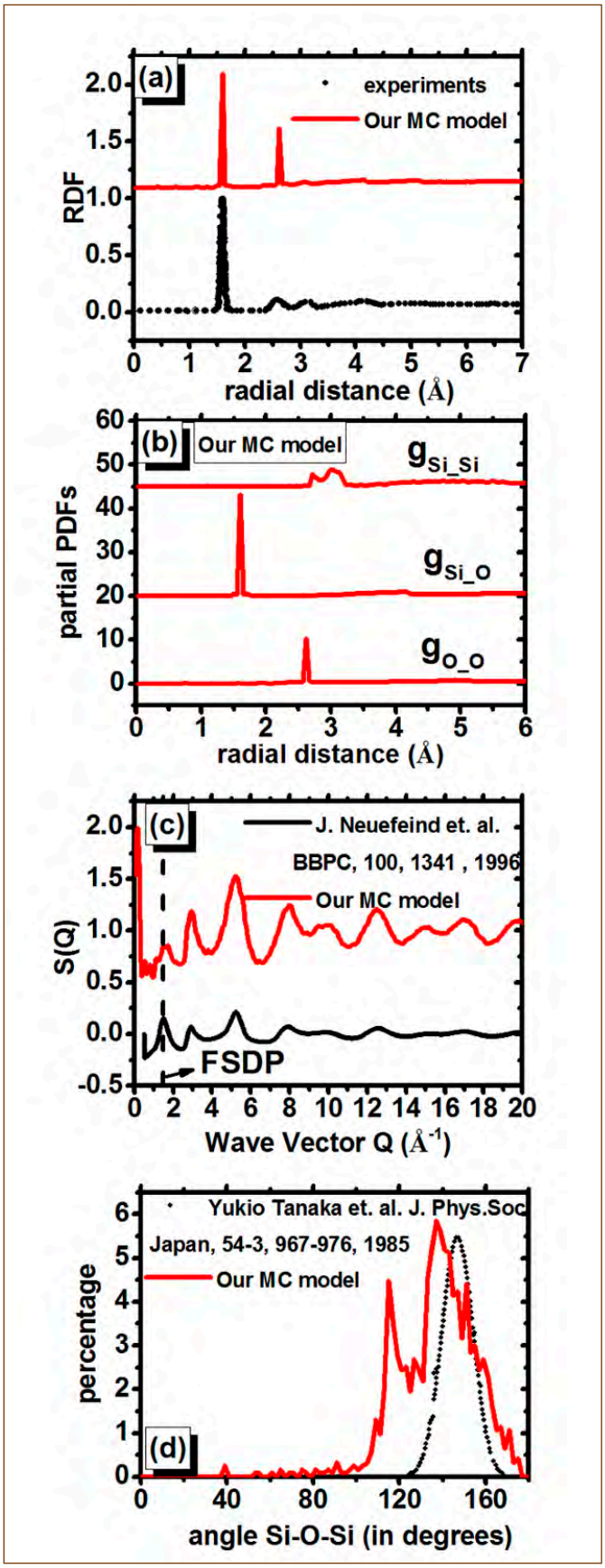

Figure 4: Comparing the (a) RDF (b) Partial pair distribution functions (c) Neutron structure factor S(Q) and (d) Bridging bond angle Si-O-Si distribution respectively of MC developed structure with experimental values

most experimental methods to quantify this order in glasses is because of the randomness involved in manner in which the basic constituent unit defined at short length scales are connected with each other. Yet there is growing consensus that the first sharp diffraction peak (FSDP) observed universally in the diffraction pattern of glasses is due to the characteristic intermediate-range clusters found in all glasses. FSDP in structure factor is the only property at intermediate length scales that can be obtained experimentally. Apart from this, Ring size distribution in glasses is also a tool to study the order/disorder at this length scale but till now no experimental tool is designed to give information about this topological aspect in glasses.

3. Long-range structure analysis: The long-range properties such as density and void distribution form essential boundary conditions on any glass model. Any structure that has significant deviation in density from what is observed experimentally cannot be claimed to be a correct structural model.

The structure of glass is so complex that one cannot reproduce properties at higher length scale without successfully reproducing the properties at lower length scales. So the analysis just described must be followed in a stepwise manner starting from the short length scales. For the silica glass model developed using the MC based code, the properties listed above are all compared with existing atomistic models (developed using DFT and RMC) and experimental values wherever available. Reported in this article are only the MC model values and the experimental curves for silica. Shown in Figure 4 are graphs for radial distribution function (RDF), partial-pair distribution function, neutron structure factor S(Q) and inter-tetrahedral bond angle distribution.

The RDF comparison in Figure 4(a) clearly shows a good agreement between the MC model and experiment. The first peak at 1.59 Å is due to the Si-O bond length followed by second peak at 2.6 Å which is the O-O distance in the tetrahedral motif. The third peak (not clearly visible due to scale) at about 3.05 Å, due to the Si-Si distance between neighbouring tetrahedral motifs. This peak was easily identified in partial pair-correlation function g_Si-Si(r) graph (Figure 4(b)). Moreover due to the randomness involved in the orientational dof of the tetrahedral motifs, the g_Si-Si(r) curve has broader peak. Subsequent peaks in RDF of this glass are suppressed due to the random structure beyond this range and hence cannot be ascertained. Due to this randomness, a glassy structure warrants that RDF should approach 1 sufficiently fast with radial distance and this happens at ~5 Å onwards in the developed structure.

In Figure 4(c), neutron structure factor S(Q) is compared. The presence of FSDP at small wave vector Q (shown by dotted line at ~1.5 Å^{-1}) is a crucial confirmation of intermediate-range order in a glassy structure which will be discussed later. Also,

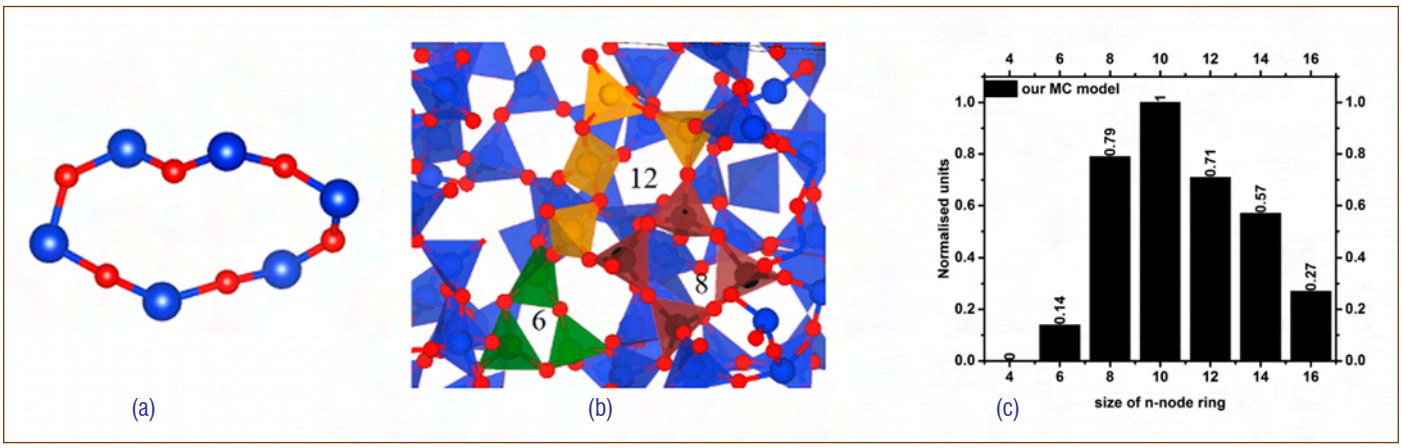

Figure 5: Ring analysis (a) image of a 12-atom ring present in the developed structure (b) snapshot of the structure showing presence of various ring size in the system (c) the distribution of rings with respect to their size in the MC model

S(Q) of the MC model and from experiment shows one to one correspondence among all the peaks, validating the structures produced by the code.

Figure 4(d) shows the inter-tetrahedral bond angle Si-O-Si distribution which is an important measure to quantify order among disorder structures. This angle is found to vary between 120° to 180°, and the distribution has a peak at ~147° observed experimentally. The MC based model shows this peak at ~140° which is slightly on the lower side as compared to the experimental value. This was due to lower cut-off constraint given in the code for this bond-angle.

After characterising the short-range structure, next step is to analyse intermediate-range structure. Figure 4(c) shows the FSDP in neutron structure factor S(Q) shown by dotted line at Q value of ~1.5 $Å^{-1}$. The presence of this peak in the MC model confirms the presence of medium range order in the structure. A quantitative analysis of the FWHM of this peak was done by fitting it with a Lorentzian function to estimate the coherence length (coherence length L=7.7/FWHM) which this peak corresponds to. In SiO_2 glass, rings of type -Si-O-Si-O- are present due to its network structure and unlike Beta-crystobalite, glass has a distribution of ring sizes around a peak value which occurs at 12-node ring size. The peak in FSDP may be related to the intermediate-range order that these rings impart to glass. The coherence length from FSDP in S(Q) of the MC model is ~12 Å which is in good agreement with experimental value of ~14 Å . For comparison, the coherence length of crystalline form of SiO_2 having similar density as silica glass, i.e. β-crystobalite form is 16 Å. The coherence length for glassy models should be less than that for crystalline forms, and this is observed for the MC model.

Rings: The structure of glass at intermediate length scale is full of facts unexplored experimentally since none of the probes available at present are able to measure any property which can be correlated to it. Nevertheless, there is increasing consensus among modelling experts that topological disorder of the glass network can be quantified in terms the rings size distribution. An irreducible ring in the context of glasses is defined as smallest closed chain/path formed by the bridging oxygen atoms and network formers, starting and ending at the same atomic site in the glassy network. In counting such rings, care should be taken to omit those rings that can be decomposed into two or more smaller rings. The size of a ring refers to the number of atoms involved in path of the ring. Out of the many possible definitions of a ring inside a structure, Guttman's shortest path criterion has been used to define a ring. According to it, starting from a node, a ring corresponds to the shortest path which comes back to the given node from one of its nearest neighbours. Figure 5 shows (a) 12-atom ring present in the developed structure and in (b) a snapshot of various rings present in the structure. In crystalline forms of SiO_2, one finds the presence of only single sized rings. For example in coesite form of silica only 8-node rings are found, keatite has 10-node, rest of the forms like quartz, crystobalite and tridymite have 12-node rings only. In contrast, silica glass structure possesses a distribution of ring sizes from 6 to 16-nodes. Shown in Figure 5(c) is the distribution of rings in the MC based model. It is to be noted that the distribution peaks near 10-12 node ring. The graph dips on either side of this ring size. This topological behaviour is confirmed in independent studies on ring statistics in SiO_2 system using theoretically derived models.

Finally for long-range structure analysis, the density and void fraction (VF) of the generated models have been compared with experimental values. The density of MC model is 2.1 g/cc which is in close agreement with the experimentally reported value of 2.2 g/cc. The VF of the model is found to be 0.30 which is different from VF obtained using Positron Annihilation Lifetime Spectroscopy (PALS) i.e. 0.18. For confirming the VF, silica glass models generated from RMC method and from DFT based

method, have been used to calculate VF. The values found for these structures are 0.29 and 0.31 respectively, which agrees well with VF of the MC model. The reason why these values are not agreeing with the experimental value may be due to the radius chosen for void calculation. For void calculation in the theoretical models considered here, the Van der Waal's radius of atom is considered. The PALS technique may be probing only a fraction of the available void space inside a material.

The agreement between structural properties of the developed model and the experimental data shows that the present method can indeed produce good structural models using minimum information about the system. But the real success of this method lies in its extensibility to more complex glass structure. So the code was redesigned to develop Iron Phosphate glass (IPG) models. The aim is to provide good atomistic models for simulation studies (DFT as well as MD) of these glasses which are presently lacking.

Modelling the IPG structures

The algorithm is extended for $40Fe_2O_3{:}60P_2O_5$ (by weight %) composition of IPG. This glass is currently being studied extensively for vitrification of waste generated during reprocessing of fast reactor spent fuel. IPG modelling poses several challenges as detailed below:

(1) The motifs involved now are phosphate tetrahedral units $(PO_4)^{3-}$, $(FeO_6)^{9-}$ octahedral and $(FeO_4)^{5-}$ tetrahedral units (having Fe in 3+ oxidation state) and $(FeO_4)^{6-}$ tetrahedral units and trigonal prism units (having Fe in 2+ oxidation state). The presence of iron in 2+ oxidation state depends on the experimental conditions of manufacturing the IPG like the melting temperature, atmosphere, quenching time and technique used. In the literature, compositions of this glass having Fe^{2+}/Fe in range 0% to 20% are studied. In the program that has been developed, the concentrations of various species can be specified in the beginning. The presence of these motifs in this composition has been studied experimentally through spectroscopic techniques as well as computational techniques like DFT and MD.

(2) The way motifs are connected to each other is also complex in IPG since various possible connections are proposed. The models developed by us have the following connectivity formalisms:

(i) The phosphate tetrahedral units share their oxygen atoms with four units of iron either octahedral or tetrahedral. Similarly, the iron polyhedral units share their oxygen atoms with phosphate tetrahedral units.

(ii) Also seen is the presence of $(P_2O_7)^{4-}$ dimer units in IPG. The superior chemical durability of IPG is attributed to the presence of these P-O-P bonds. The percentage of such connections is about 30-40 %. This is also taken care of in the modelling.

(iii) Fe^{2+} coordination is not conclusive from any study but there are studies which claim that $Fe_3(P_2O_7)^2$ crystal has most resemblance with IPG structural connections. So Fe^{2+} is modelled to be in face sharing structure with Fe^{3+} octahedral in a distorted geometry.

(iv) Effectively one has $(Fe_3O_{12})^{16-}$ clusters interconnected via

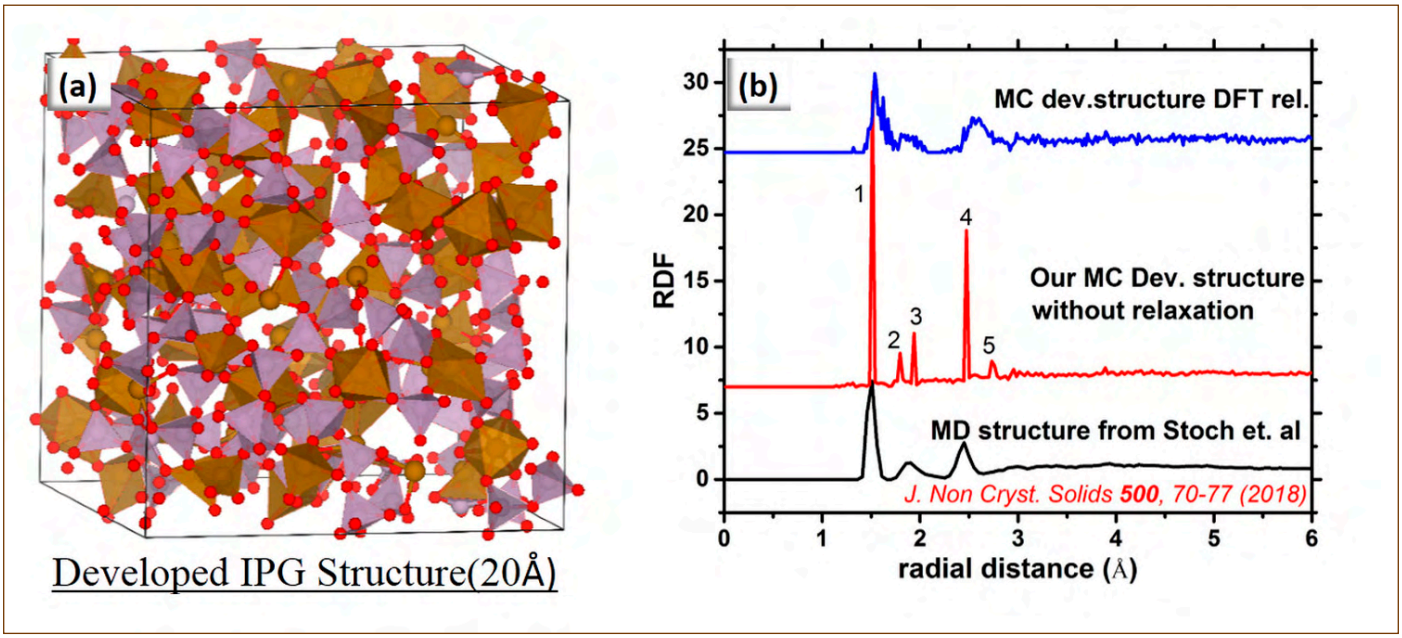

Figure 6: (a) The developed structure of IPG using MC method (b) the RDF of MC developed structure before and after DFT-relaxation as compared with an MD model from literature. Curves are stacked for clarity

Table 1 showing effect of DFT relaxation of model developed using MC method on Coordination number (CN) of each constituent, Density and total energy per atom of the structure; U: Unrelaxed, R: Relaxed

Developed Structure of IPG		O CN (2)	P CN (4)	Fe CN (6)	Density (g/cc) (2.9)	Energy change upon relaxation (eV/atom)
Structure 1	U	1.74	3.41	5.52	2.94	-0.16
	R	1.92	3.97	5.76	3.02	
Structure 2	U	1.72	3.58	5.95	2.77	-0.10
	R	1.78	4.0	5.68	2.77	
Structure 3	U	1.97	3.53	5.84	3.19	-0.15
	R	2.07	3.86	5.92	3.29	
Structure 4	U	1.83	3.42	5.96	3.16	-0.11
	R	1.93	3.89	5.87	3.15	
Structure 5	U	1.74	3.81	5.58	2.72	-0.10
	R	1.79	3.94	5.74	2.85	

$(P_2O_7)^{4-}$ dimer and $(PO_4)^{3-}$ monomer units. The percentages of these units vary according to composition and preparation conditions.

In the composition adopted for modelling (which is reported to be most durable) the following distribution of the units is observed: Fe/P ratio is 0.67 from the formula. P exists mostly in $(PO_4)^{3-}$ tetrahedral form (~100%) due to its strong covalent character. Fe exists in two oxidation states +2 and +3. The ratio of Fe^{2+}/Fe is found to vary from 0 to 20%. Fe^{2+} exists in distorted octahedral or trigonal prism geometry having face sharing with the Fe^{3+} octahedral unit. Fe^{3+} is found to exist in two geometries i.e. octahedral (75%) and tetrahedral (25%). Hence average coordination number for Fe is between 4 and 6.

The developed structure is shown in Figure 6(a). The simulation cell is a cube of edge 20 Å containing 411 O atoms, 114 P atoms, 78 Fe^{3+} atoms and 9 Fe^{2+} atoms. In total the structure has 612 atoms. The density of the developed structure is 3.1 gm/cc (experimentally IPG has 2.9 gm/cc). The structure is compared with the MD developed structure by Stoch et.al (J. Non Cryst. Solids 500, 70-77 (2018)) on the basis of structural properties as it was done for silica glass. Also presented are the structural properties of the developed structure after force-relaxation using DFT. The need and implications of this is discussed separately later on.

In Figure 6(b) the comparison of RDF of the structures is also shown. Note that the RDF produced by the developed structure matches well with that of the MD developed structure. These peaks are identified with the following bond distances present in the structures. Peak 1 corresponds to P-O bond distance of 1.51 Å present in PO_4 tetrahedral motif. Peak 2 and 3 corresponds to Fe-O bond distances of 1.80 Å and 1.94 Å present in tetrahedral and octahedral motifs respectively. Peak 4 and 5 corresponds to O-O bond distance of 2.48 Å and 2.74 Å present in PO_4 tetrahedral and FeO_6 octahedral motifs respectively. The peak corresponding to O-O bond distance of 2.95 present in FeO_4 tetrahedral unit is considerably subdued in intensity due to lesser number of such units present in the structure.

Coordination number analysis: There are three coordination geometries to be considered here. First is the average coordination number of oxygen in the structure. For a perfect structure we expect this to be 2, since oxygen acts as bridging atom between Fe and P or between P and P in the network. For the developed structure this is found to be 2.32 having average P contribution of 1.07 and average Fe contribution of 1.25. The Fe contribution is more due to the presence of edge-sharing distorted pyramidal units with Fe^{2+} sitting in them. This is found missing in the MD structure which has average coordination number for O as 2.11 with 0.98 contribution from Fe and 1.13 from P. Second is the coordination geometry of P in the structure. Since $(PO_4)^{3-}$ has strong covalent character, ideally the average coordination around P should be 4. In the developed structure we have this number to be 3.87 which also compares closely with the value of 3.89 obtained for the MD structure. Finally, the third coordination is that of Fe. From the literature, Fe is known to be present in both tetrahedral and octahedral environments, with Fe^{2+} favouring a distorted octahedral geometry. Thus, the coordination is expected to be less than 6 for Fe in IPG structure due to its ionic character. The value of average coordination number for Fe in the developed structure is found to be 5.89. The value for MD developed structure is found to be 5.04.

Apart from this, detailed analysis is also done for other structural properties such as partial pair-correlation function, bond angle distributions, void fraction and density comparison. The agreement between structural properties of model developed from the code versus structures developed using MD shows that the code can be applied for modelling complex glass structures

as well. Moreover, the topology information from experiments can be designed into the code to produce the required coordination among units. This sets the present method apart from other available methods mentioned earlier which rely heavily on crystal structures as starting structures.

The peaks in RDF of the developed structures are more sharply defined due to the use of rigid motifs and absence of force-relaxation in the presented method. The peaks become broader and glass-like after DFT relaxation (see the RDF coloured in blue in Figure 6(b)), which is expected. The point to be emphasized here is that though a force relaxation is necessary after modelling any glass structure, still the time taken for relaxation of forces can be orders of magnitude smaller if the starting structure is closer to the metastable valley in PEL in which the glass actually resides. Also modelling the key structural aspects through coding helps the relaxation to find the correct metastable valley from the sea of possible valleys in PEL. For validating this point, some structures of IPG were developed and relaxed using DFT. These results are presented next.

For studying the effect of relaxation, 5 structures of IPG having composition $40Fe_2O_3{:}60P_2O_5$ with 0% Fe^{2+} were developed. For force relaxation a strategy appropriate for glasses is adopted where the individual atoms might still be allowed to have some small forces due to the quenched-in disorder but the overall structure should have zero net force. DFT-VASP package is used for carrying out the structural relaxation. Since the structures have around 200 atoms without any symmetry, so only gamma point calculations are carried out with ENCUT=450eV. Thereafter ionic position relaxation and cell volume relaxation were carried out successively many times till net force on all the atoms falls below 0.1 eV/Å.

The result of this exercise is summarised in Table 1. After relaxation the coordination numbers approach to their perfect values (written in brackets). The perfect values may never be attained in a realistic structure due to the presence of coordination defects in glasses. The effect of relaxation on density and energy of the structure is also recorded. The last column shows the energy per atom gained upon relaxation. The negative values in all the developed structures show the correctness of the relaxation approach adopted for glasses. Also, the data in the table shows the progress of the structure towards the metastable valley in PEL. Here only the structural aspect of generated models is discussed, but we are also currently studying the physical and mechanical properties of generated structures using both DFT and MD.

In summary, a recipe is presented for developing glassy structures which is extensible to complex glasses like IPG and can generate large scale structures utilizing only short-range properties and connectivity information that is apriori available from experiments. But the advantage of not requiring inter-atomic potentials necessitates that the structures be relaxed using DFT/MD depending upon their scale. The necessity of such atomistic models is immense in the current scenario where simulation based studies of amorphous and glassy materials require such structures as the first step in their analysis.

Reported by Shri Shakti Singh
Materials Physics Division, Materials Science Group

Young Officer's FORUM

Dr. Ch. Kishan Singh is working as a Scientific Officer at Surface Science section, SND, MSG, IGCAR. He acquired his master's degree from University of Pune. He worked as a CSIR-NET JRF before joining IGCAR as SO/C in Feb 2010. He obtained his Ph.D from HBNI in 2015 under the guidance of Dr. A. K. Tyagi. His basic research interests are materials science of thin films and the investigation of associated surface and interface related phenomena at various length scales.

Metal Induced Crystallization of Group-IV Elemental Semiconductors and their Alloy Thin Films on Glass at Low Temperatures

A number of exciting low-thermal budget applications are envisaged based on the realization of polycrystalline (poly)-Si, Ge and SiGe thin films on low-cost non-crystalline insulating substrates like glass, plastics and polymers (polyimide). To name a few, this includes high-performance flexible electronics, high-speed thin-film transistors (TFTs), high-efficiency solar photovoltaics and advanced flat panel displays. The technological challenge herein lies not only in growing a crystalline template on the aforementioned amorphous substrates but doing so below the softening temperature of these substrates (~ 170 to 370 °C); the bulk crystallization-temperatures (T_{cryst}) of Si, Ge and SiGe are much higher and above 500 °C. In order to circumvent these challenges, several efforts have been made to reduce the T_{cryst} of the semiconductor (SC). Among them, metal-induced crystallization (MIC), wherein a metal in contact with an amorphous (a)-SC catalytically lowers the T_{cryst} of the latter, has gained widespread attention because, in addition to reducing the T_{cryst}, MIC can enable a controlled growth of large grains in the resulting thin films. MIC phenomena can be described as interfacial thermodynamics controlled solid-state phase transformation driven by lowering of the overall Gibb's free energy and involves a delicate balance of various surface and interface energies. While several transition and post-transition metals promote MIC of amorphous a-Si (and a-Ge), crystallization catalyzed by transition metals (except Ag and Au) occurs via the formation of a compound phase (silicides or germinides) and the lowering of T_{cryst} is only moderate. On the other hand, Ag, Au and the post-transition metals (like Al)

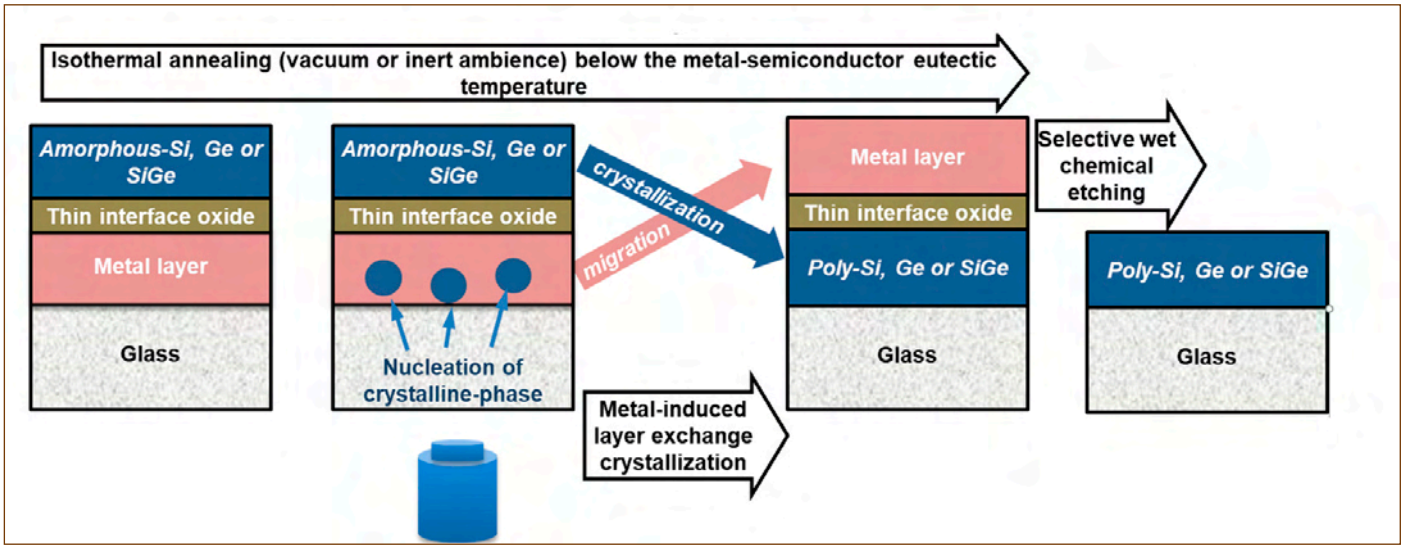

Figure 1: Schematic illustration of metal-induced layer exchange crystallization process

form binary eutectic systems with Si (and Ge), and the T_{cryst} lowers significantly from their bulk values, particularly with Au and Al. Further, as the metal and poly-SC remain phase segregated in MIC with eutectic systems, the migration of the metal phase caused by the crystallization dynamics may lead to the exchange of the metal and SC original layer positions. In such cases, the MIC process can be controlled to enable the growth of crystalline template, i.e., poly-Si, Ge or SiGe, directly on amorphous substrates. The schematic illustration of such a process is given in Figure 1 and it is known as the metal-induced layer exchange (MILE) crystallization process.

A MILE crystallization process starts with a thin film stack on a substrate (usually glass), as shown in Figure 1 (leftmost). The thicknesses of the a-SC and metal layers in the stack are preferably kept under 100 nm as MIC is a localized interface controlled phenomenon. Additionally, the thickness ratio is maintained roughly at 1:1, the a-SC layer's thickness can be kept slightly higher. The stack undergoes a layer exchange phenomenon from the original a-SC/metal to a metal/poly-SC bilayer on glass upon isothermal annealing in either vacuum or N_2 ambient. The reason for the layer exchange is related to crystallization induced strain and is elucidated later on. The annealing temperature (T_a) is set below the metal-SC's eutectic temperature (T_e) to ensure the system remains in a solid phase throughout the process and no alloying occurs. A thin oxide layer is introduced at the metal/SC interface to limit the diffusion of the SC atoms into the metal layer. This interfacial diffusion limiting (IDL) layer controls the nucleation density of crystalline-SC grains in the metal layer and leads to a large-grained poly-SC thin film. The microstructure and the thickness (usually ~ 2 to 4 nm) of the IDL layer also affect the kinetics of the MILE process. The nucleation of crystalline SC grains in the metal layer and subsequent grain growth is directly visualized from the backside of the glass substrate, as shown in Figure 1. The time evolution of the grain growth so acquired can be used to extract information about the crystallization kinetics. Further, the microstructure of the metal layer, particularly the grain boundaries (GBs), plays a vital role in enabling and retarding MIC and MILE, as will be briefly discussed later. Finally, after the MILE crystallization process, the top metal layer is removed by a selective wet chemical etching to leave only the poly-SC on the glass. Diluted HCl (at 60 °C) and KI/I2 (4:1 ratio) solutions are used to etched Al and Au, respectively. For applications that warrant thicker films, the poly-SC realized through MILE can be used as the crystalline template for further epitaxial thickening.

As both the MIC and MILE depends on several parameters, it is impossible to determine a unique combination of these parameters that result in the lowest T_{cryst}. Even if there were one, the resulting T_{cryst} would vary according to the inevitable microstructural variation of the films in the stack unique to each technique and equipment used for deposition. Hence, the quest for the lowest achievable T_{cryst} is far from over and still on. Herein this report, the findings of MIC and MILE in the following metal-SC eutectic systems viz, Au/Ge, Al/Ge, Au/Si and Al/SiGe, are briefly presented. The deposition of all the thin films in the stack (except Au thin films, which were DC sputtered) was performed in a custom-built electron (e)-beam evaporator equipped with a 3 kW (single pocket) and 8 kW (multi-pocket) sources. The base pressure and working pressure was 10^{-8} and 10^{-7} mbar, respectively. The isothermal annealing was performed either in a vacuum (10^{-8} mbar) or a custom-built gas flow furnace (UHP N_2 gas at a flow rate of 5-10 sccm). The vacuum annealing was performed in a Eurotherm heater assembly attached to the substrate manipulator (UHV-Design) of the e-beam evaporator.

Al-Ge system

The Al-Ge system has a $T_{e(Al-Ge)}$ ~ 420 °C and hence, Al-induced crystallization (AIC) are performed at T_a in the range 300 to 400 °C,

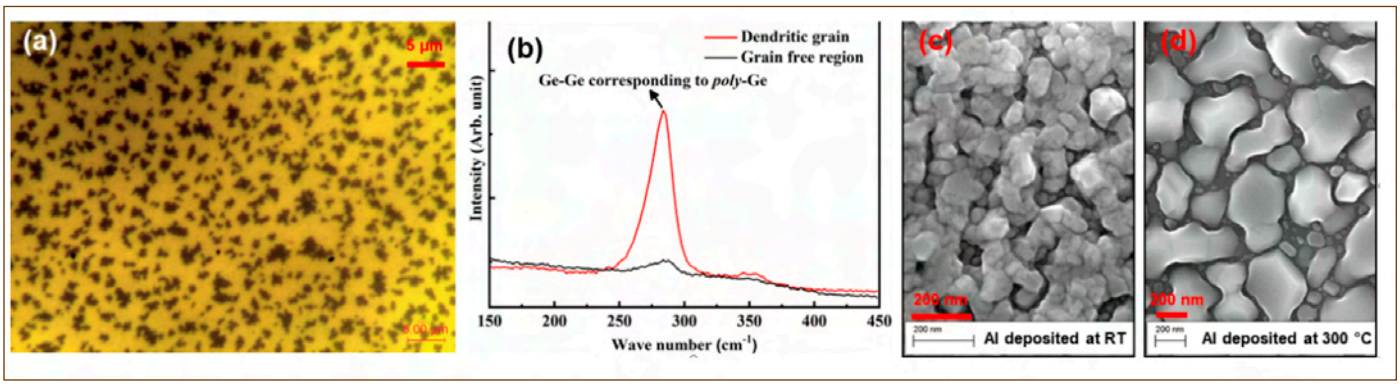

Figure 2: (a) Optical micrograph of stack-1 after annealing at 300 °C for 100 h in N_2 ambient (b) Raman spectra from different regions of annealed stack-1. FE-SEM micrograph of Al deposited at (c) RT and (d) 300 °C

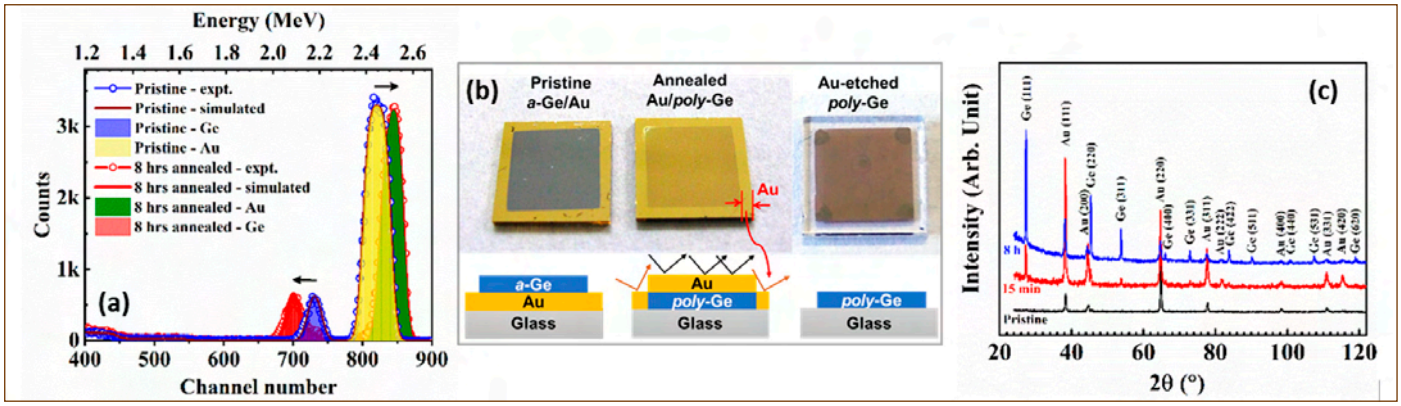

Figure 3: (a) RBS spectra of the pristine and annealed samples (b) Image of the pristine, annealed and Au-etched samples (c) GIXRD of the pristine and annealed samples

lower than both the $T_{e(Al\text{-}Ge)}$ and the bulk $T_{cryst}(Ge) \sim 500$ °C. The results obtained from two stacks with different structure is presented. The first stack (stack-1) has $\{a\text{-}Ge(25\ nm)/Al(5\ nm)\}_{\times 2}/GeO_x$ ($\sim$2 nm)/Al(40 nm)/glass structure such that the overall Ge:Al $\sim$ 1:1. The lowest T_a at which this stack starts exhibiting MIC is 300 °C. The optical micrograph obtained from the backside of the glass showing the growth of dendritic Ge grains on the glass substrate is presented in Figure 2. While such growth indicates the initiation of layer exchange phenomenon, the crystallinity of these grains were confirmed by Raman spectroscopic measurement, also acquired through the glass substrate (with 514 nm laser source) as shown in Figure 2. On the other hand, the second stack (stack-2) with a-Ge(50 nm) /AlO_x($\sim$1-2 nm)/Al(50 nm, 300 °C)/glass structure, shows no observable nucleation of poly-Ge grains on the glass sample even after annealing at $T_a = 400$ °C. The grazing incidence X-ray diffraction (GIXRD) of the annealed stack-2 (not shown) however show weak peaks indicating the formation of nanocrystalline-Ge phase. These observations, which highlight the crucial role of metal GBs (i.e., metal/metal interface with an energy γGB) in the crystallization and layer exchange process, can be explained by understanding the underlying physical mechanism of MIC, discussed next.

The driving force for MIC is the minimization of Gibbs free energy (G) as the crystalline phase of an SC has a lower G than the amorphous phase. However, a barrier prevents the spontaneous nucleation of the crystalline phase. The primary mechanism through which this barrier is surmounted involves a covalent bond weakening of the SC atoms in contact with a metal due to electronic screening by the metal's free electrons. This weakening is a very localized interface phenomenon affecting only about a few monolayers of the a-SC phase and facilitate the SC atoms in the interface region to become mobile at temperatures much below its bulk T_{cryst}. These mobile SC atoms are then free to diffuse along the metal/SC interface or into the metal GB. Subsequent nucleation of a c-SC phase occurs when the lowering in G due to crystallization can overcompensate the energy penalty for creating new surfaces (γ^s) and interfaces (γif) upon such crystallization. The interface energetics are considered in the following manner: - i) If the c-SC nucleates at the SC/metal interface, such interface is replaced by two new interfaces viz, c-SC/a-SC and c-SC/metal. Energetically, the interface energy (γ^{if}) increase by ($\gamma^{if}_{c\text{-}SC/a\text{-}SC}+\gamma^{if}_{c\text{-}SC/metal}$)-$\gamma^{if}_{a\text{-}SC/metal.}$ ii) If the SC atoms wet the metal GB and c-SC nucleate there, such GB will be replaced by at least two c-SC/metal interfaces. Accordingly, the increase in γ^{if} is given by ($2 \times \gamma^{if}_{c\text{-}SC/metal}$)-$\gamma^{GB}_{metal}$ and so on.

The FESEM micrographs of the Al thin film deposited at room temperature (RT) which is the metal layer in stack-1 and 300 °C (the metal layer in stack-2) are shown in Figure 2(c) and (d). The Al film deposited at RT exhibits fine grains microstructure and has a high density of GBs. In stack-1 with such Al film, the driving force for the mobile Ge atoms to wet the Al GBs given by the difference $\gamma^{GB}_{Al} - 2 \times (\gamma^{if}_{a-Ge/Al}) > 0$ i.e., positive. As a result, the mobile Ge atoms generated at the a-Ge/Al interface during isothermal annealing diffuse into the Al GBs and nucleation of c-Ge occurs either at the GB or the glass substrate. Once nucleated, the c-Ge grain grows with the steady supply of mobile Ge atoms from the a-Ge/Al interface region via GB diffusion, ultimately leading to the layer exchange. This process is refer to as Al-induced layer exchange (ALILE) crystallization process. In contrast, the Al film deposited at 300 °C exhibits an equiaxed like isolated grains (as large as $\sim$ 400 nm) with gaps between them measuring $\sim$ 50 to 400 nm. The consequence of this growth is the lack of Al GBs and effective reduction of the a-Ge/Al interface area in stack-2. It not only retards the crystallization by limiting the catalytic AIC to the Ge/Al interface region alone but suppresses both the GB diffusion of Ge atoms and subsequent layer exchange that would enable a direct growth of poly-Ge on a glass substrate.

Au-Ge system

The Au-Ge system has a low $T_{e(Au-Ge)}$ ~ 361 °C and MIC with Au as the metal results in a relatively lower T_{cryst} of Ge. The lowest T_{cryst} that are reported for Ge with Au-induced layer exchange (AUILE) crystallization process is in the range of ~ 250 to 275 °C. This T_{cryst} is effectively lowered to ~ 170 °C by employing vacuum annealing in an optimized stack with the following structure :- a-Ge(50 nm)/ GeO_x(~ 2 nm)/Au(50 nm)/glass. The GeO_x layer was formed by deposition of ~ 2 nm Ge thin film and intentionally exposing it to ambient for a duration of 30 to 60 min. The experimental observation of layer exchange phenomenon is presented in the Rutherford backscattering spectrometry (RBS) spectra of the pristine and annealed samples shown in Figure 3(a). Compared to the pristine sample, the RBS spectra of the annealed sample shows a complete shifting of the Au and Ge peaks to higher and lower channel number (read energy), respectively. The images of the pristine, annealed and etched sample is shown in Figure 3(b). The structural phase of the layer exchanged Ge is confirmed as poly-Ge phase from the GIXRD pattern shown in Figure 3(c).

The interface energetics for a-Ge/Au bilayer is briefly discussed to explain the very low T_{cryst} observed in this case. The Au thin film sputter deposited at RT has good polycrystallinity, as evident from the GIXRD pattern (Figure 3(c)). It contains a considerable density of high-angle GB with an average energy γ_{Au}^{GB} ~ 450 mJ-m^{-2}. The interface energy of a-Ge/Au system ($\gamma_{(a\text{-}Ge/Au)}^{if}$) on the other hand, is calculated to be ~ 3 mJ-m^{-2} at 170 °C. Hence, a large driving force exists for wetting the Au GBs by the mobile Ge atoms at a temperature as low as ~ 170 °C. In addition, while the lattice diffusion of Ge into Au at 170 °C i.e., 0.16 × T_m(Au) (melting point of Au) is non-existent, the estimated GB diffusion coefficient of Ge into Au is estimated to be quite large ~ 5 × 10^{-12} cm^2-s^{-1}. Once the a-Ge atoms wet the Au GB via GB diffusion, the a-Ge phases at the Au GB will be stable till it reach a thickness wherein the reduction in G from crystallization can compensate for the creation

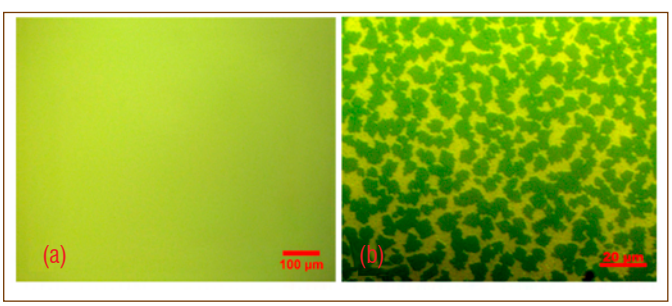

Figure 4: Optical micrographs of: - (a) a-Ge(50 nm)/GeO_x(~ 2 nm)/ Au(50 nm, 360 °C for 4 h)/glass after annealing for 16 h and (b) a-Ge(50 nm)/GeO_x(~ 2 nm)/Au(50 nm, 240 °C for 4 h)/glass after annealing for 1 h

of more energetic c-Ge/Au interfaces. This thickness is estimated to be a few monolayers. Once the a-Ge at the Au GB exceed few monolayers, c-Ge nuclei nucleates at the GB. These c-Ge nuclei then grow with the steady supply of Ge atoms from the interface region via GB diffusion. However, as growth along the vertical direction is limited by the Au thin film (~ 50 nm), the c-Ge grains grow laterally along the in-plane direction thereby asserting strain to the Au layer. In addition, since Au has a higher thermal expansion coefficient (TEC) and smaller lattice parameter (*a*) compared to Ge, the thermal strain due to c-Ge/Au interfaces is compressive in the Au lattice. Consequently, Au undergoes a strain relieving migration to the top position earlier occupied by a-Ge, leading to the layer exchange phenomenon. The origin of the layer exchange is explained in detail later using in-situ stress measurement (with XRD method) during ALILE in the Al-SiGe system.

To further validate the significant role of the Au's GB in enabling AUILE crystallization at 170 °C, the Au film was pre-annealed at 360 °C, i.e., 0.34 × T_m(Au) for 4 h under vacuum (~10^{-8} mbar) before the deposition of IDL and a-Ge layers in another stack. This stack was subjected to the same isothermal vacuum annealing at ~ 170 °C and no AUILE could be observed even after 16 h as shown in Figure 4(a). Upon pre-annealing, the GB density of Au reduces drastically due to re-crystallization, wherein all the high angle GB get subsumed and only a small low-angle (i.e., low energy) GB remains in the film. Consequently, the driving force for wetting the Au GB reduce and no diffusion of Ge atoms or AUILE crystallization could occur. However, if either the pre-annealing duration or the temperature of the Au film is reduced, some fraction of high angle GB survives the partial grain growth. In such a case, there exists enough driving force for Ge atoms to wet the Au GB, subsequently leading to AUILE crystallization. Such optimization can be gainfully exploited to grow large-grained Ge as the reduction of nucleation density enable the Ge grains to grow larger, as shown in the optical micrograph of Figure 4(b).

Finally, a poly-Ge thin film on glass (Figure 3(b)) is realized by removing the top Au layer employing the KI/I2 solution. An electron backscatter diffraction (EBSD) mapping of the Au-etched poly-Ge thin film showing the orientation and the grain size (lateral) distribution is shown in Figure 5. The poly-Ge film has no preferred orientation and there is a wide variation in the grain size with some measuring as large as ~ 0.8 μm. The absence of any residual Au in the etched film was then confirmed using energy-dispersive X-ray spectroscopy (EDS) measurement shown in Figure 5(c). The spectrum shows no sign from Au within the sensitivity of EDS, i.e., ~ 0.1 wt. %. The solubility of Au in Ge at 170 °C is estimated to be ~ 1.3 × 10^7 cm^{-3} using an empirical relationship as such

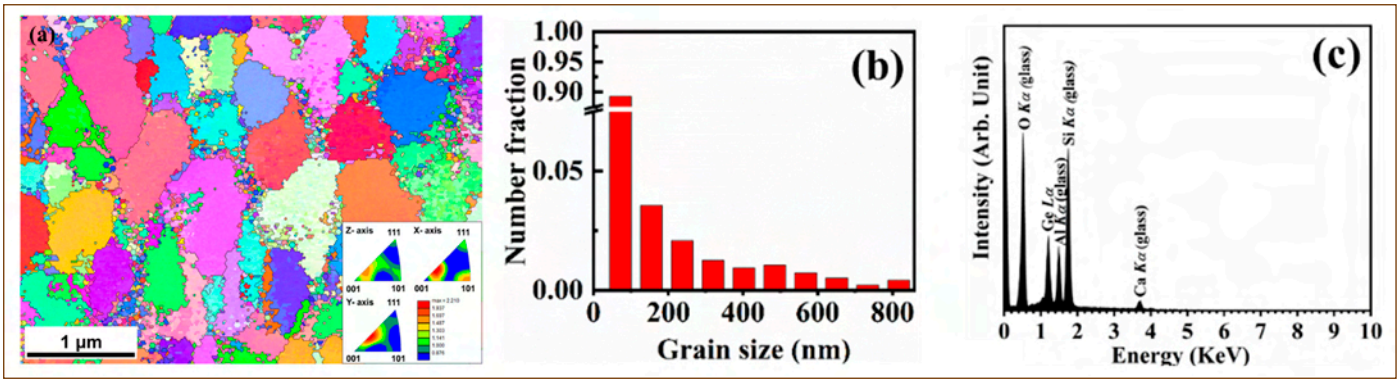

Figure 5: (a) EBSD mapping of the poly-Ge thin film; Inset: Inverse pole Figure (b) Grain size distribution and (c) EDS spectrum of the etched poly-Ge thin film

experimental data does not exist for such low temperature. The observation indicates either an effective removal of Au from the poly-Ge thin film or, if present, is in trace level. However, the poly-Ge thin film exhibits p-type semiconducting behaviour due to point defects induced acceptors states with a hole mobility ~ 50 cm^2 V^{-1} s^{-1} at RT. This result is significant because, apart from being the lowest T_{cryst} in Au/a-Ge system, it enables an effective separation of Au from the poly-Ge thin film in a real macroscopic sense that may lead to exciting applications.

Al-SiGe system

The $T_{e(Al\text{-}SiGe)}$ of the ternary Al-SiGe system depends on the stoichiometry. The lowest T_a at which ALILE crystallization occurs in a-SiGe(80 nm)/AlO_x(~ 2 nm)/Al(80 nm)/glass stack similar to the case of binary Si-Al or Ge-Al system was 350 °C, well below both the $T_{e(Al\text{-}Ge)}$ and $T_{e(Al\text{-}Si)}$. The direct nucleation of c-SiGe from a-SiGe phase without the formation of either poly-Ge or Si phase indicates no heterogeneity in the way Si and Ge atoms diffuse into the Al matrix after their dissociative breakage from the a-SiGe phase. As the AIC process is a solid-to-solid phase transformation, strain energy inherently develops at the newly formed interphase boundary. Such strain will invariably alter the stress of the thin film system. Hence, a comprehensive understanding of the ALILE crystallization process must include the strain energy while considering the overall free energy changes. For this purpose, the evolution of residual stress in the Al layer during isothermal annealing is studied using the X-ray diffraction technique. A correlation of such an evolution with the growth kinetics will then unravel the origin of the layer exchange phenomenon during the AIC process.

The optical micrographs of the annealed stack showing the onset and progress of ALILE crystallization of a-SiGe are shown in Figure 6(a). The nucleation of the c-SiGe phase/grains starts after annealing the stack in N_2 ambient for a duration (t_a) of ~ 22 h. While the full layer exchange completes in ~ 144 h of annealing, the resulting poly-SiGe thin film has an average lateral grain size of ~ 50 μm. The GIXRD patterns shown in Figure 6(b) confirm

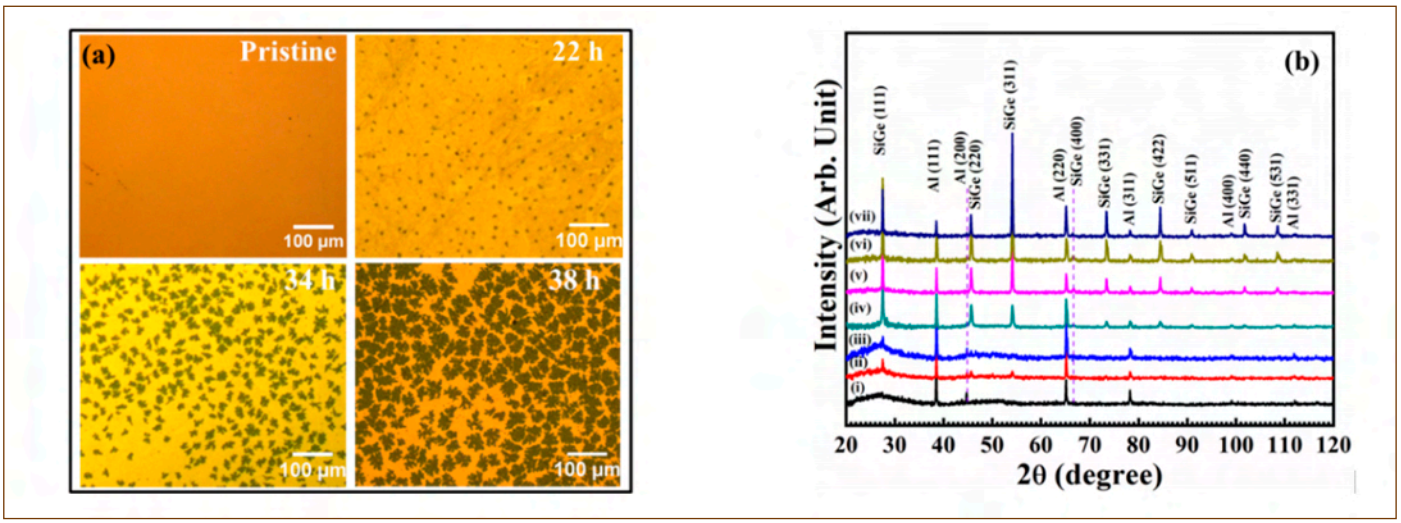

Figure 6: (a) Optical micrographs of the poly-SiGe on glass after annealing for various durations and (b) GIXRD pattern of the stack after isothermal annealing (at 350 °C in N_2 ambient) for: - (i) Pristine (ii) 22 h (iii) 24 h (iv) 34 h (v) 38 h (vi) 58 h and (vii) 144 h

the structural phase of the poly-SiGe thin film in the annealed stack. The c-SiGe nuclei/grains grow laterally as growth along the vertical direction is limited by the Al thin film ~ 80 nm. Due to the planar nature of growth, the active area covered by c-SiGe grains (measured from Figure 6(a)) gives a direct estimate of the crystallized SiGe fraction (f_{cryst}). The evolution of f_{cryst} then provides information about the kinetics of the crystallization process.

Before discussing the results on residual stress, a brief description of the methodology used is given herewith. The in-plane residual stress $\sigma_{||}$ (or simply σ) in the Al layer is estimated from the GIXRD patterns (Figure 6(b)) using a multi-*hkl* $\sin^2\psi$ technique, where ψ is the tilt of the Bragg's plane w.r.t. the sample normal and given by $\psi=\theta^{hkl}-\alpha$. Here, θ^{hkl} and α are the Bragg's angle for hkl plane and the grazing incidence angle, respectively. It must be noted that such analyses cannot be performed reliably with c-SiGe peaks, as both stress and compositional change can cause peak shifts in SiGe. In a cubic system, all the inter-planar spacings (d^{hkl}) are uniquely related to the lattice parameter (*a*) via $a=d^{hkl}\sqrt{(h^2+k^2+l^2)}$. Hence, the strain ($\varepsilon$) can be measured as $\varepsilon_\psi=(d^{hkl}-d_0^{hkl})/d_0^{hkl}=(a-a_0)/a_0$, where a_0 and d_0^{hkl} are the strain-free value of *a* and d^{hkl}, respectively. The σ is then estimated from the slope obtained by linear regression of ε_ψ w.r.t. $\sin^2\psi$ according to the X-ray stress equation (XSE): $-\varepsilon_\psi=\frac{1+\nu}{E}\sigma\sin^2\psi-\frac{2\nu}{E}\sigma$, using Poisson's ratio (ν) = 0.33 and Young's modulus (E) = 69 GPa, for Al. The value of a_0 was estimated from *a* vs. $\sin^2\psi$ plots as the value of *a* corresponding to ψ^0 for which the LHS of XSE i.e., ε_ψ = 0. Please also note that the slope of ε_ψ (or any function of *a*) vs. $\sin^2\psi$ plot will indicate the nature of residual stress in the material, which is positive for tensile and negative for compression.

The evolution of σ in the Al layer with the progress of ALILE process, indicated by t_a and f_{cryst} is given in Figure 7(a). The creation of new crystalline c-SiGe/Al interfaces increases the overall interface energy (γ^{if}), which has contribution from lattice mismatch (strain energy) and chemical interaction. Depending on where the c-SiGe nucleates, energetically the γ^{if} increase by at least $2\times(\gamma^{if}_{c-SiGe/Al}\sim 0.38\ J/m^2)-\gamma^{GB}_{Al}(\sim 0.33\ J/m^2)$. As the f_{cryst} increases, the total c-SiGe/Al interface area and the strain (or stress) contribution to γ^{if} also increases. Hence, the intrinsic growth stress in the Al layer of the pristine stack, which is tensile ~ 14.6 MPa, initially increases with increase in both t_a and f_{cryst}. During the initial 24 h of annealing, σ steadily rises from ~ 14.6 to 202.8 MPa while f_{cryst} sees only a marginal rise from 0 to ~ 4 %. Subsequently as the strain builds up, the thin film system strives to lower the overall γ^{if} by driving Al to undergo a strain relaxing migration to the voids left over by the diffusing Si and Ge atoms. This process leads to the initiation of layer exchange phenomenon as seen by the nominal increase of σ from 202.8 to ~ 233.6 MPa, whereas the f_{cryst} increase to ~ 12 %, in the next 10 h, i.e., t_a = 34 h. There is no well-defined critical threshold value of σ for the layer exchange as the ALILE is a gradual process. However, in the next 4 h, σ increase from ~ 223.6 MPa to a maximum value of ~ 325.3 MPa due to a surge in f_{cryst} from ~ 12 % at 34 h to ~ 44 % at 38 h. Further, as f_{cryst} increases at t_a > 38 h, σ decreases due to the strain relieving migration of the Al layer caused by the additional increase in f_{cryst}. This process continues till such strain induced migration reduce the total $\gamma^{if}_{(c\text{-}SiGe/Al)}$ by minimizing the c-SiGe/Al interfacial area and the overall γ^{if}. Also, the ALILE process becomes increasingly slower as f_{cryst} approaches 100 % because the Al layer now has more poly-SiGe than the original Al film.

As the ALILE crystallization is a dynamic process occurring at 350 °C, the thin film system and the strain also dynamically evolve during the process. Hence, to ensure that the measured strain is reliable, the process was interrupted after each annealing cycle and σ was measured after thermalizing the stack to RT. Note that the measured σ now consists of only thermal contribution as the intrinsic part gets

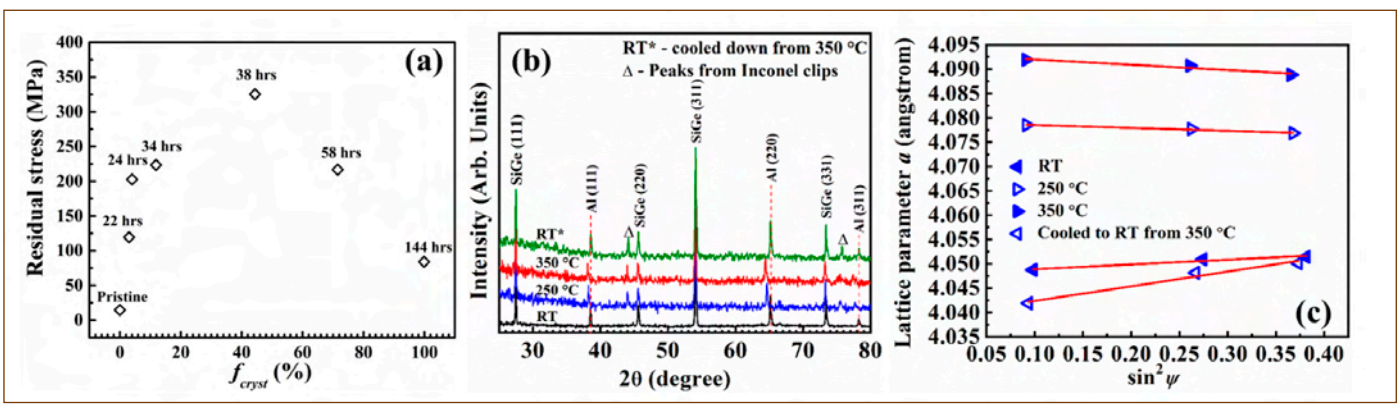

Figure 7: (a) Evolution of residual stress (σ) in the Al layer (measured at RT) w.r.t. the crystallized phase fraction (f_{cryst}) and annealing duration (b) in-situ high temperature GIXRD pattern of the 144 h annealed stack and (c) ψ-dependence of *a* for the 144 h annealed stack

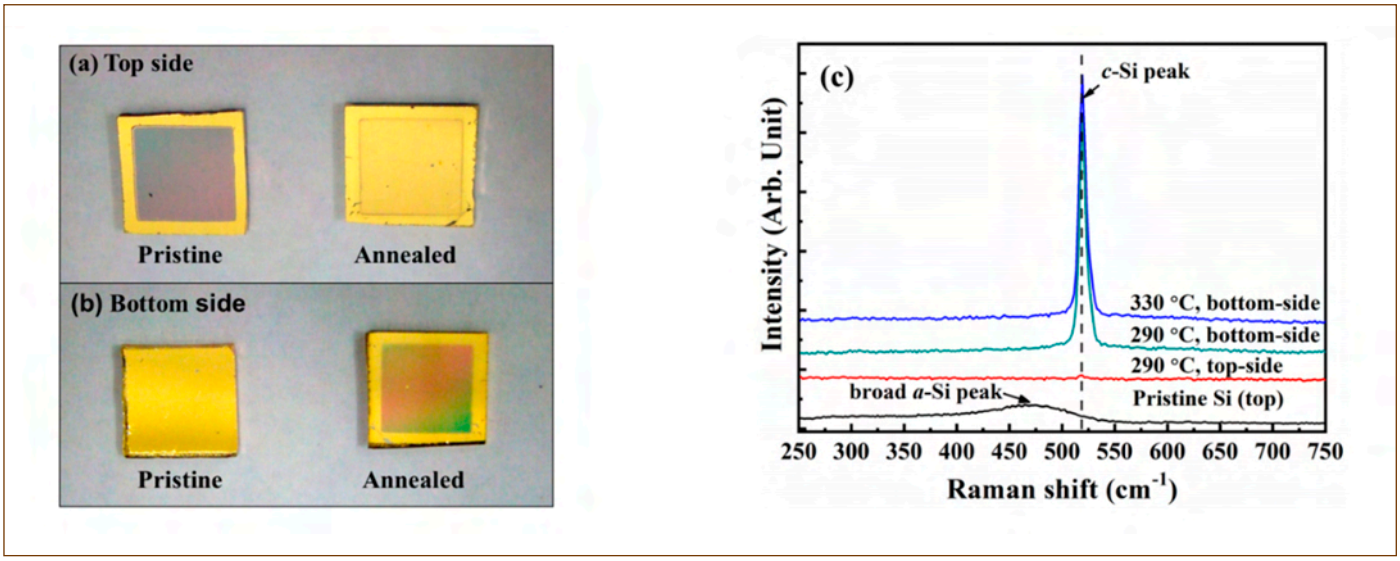

Figure 8: Image of the pristine and the annealed stack after annealing at 290 °C for 6 h acquired from: (a) top side and (b) bottom side. (c) Raman spectra of the pristine and the annealed stack after annealing at different temperatures for 6 h

relieved upon prolonged annealing at high T_a. Also the tensile value of σ for Al at RT indicates compressive stresses in the Al lattice at high T_a (350 °C) as SiGe has a larger *a* but a lower average TEC than Al. This inference is confirmed by in-situ elevated temperature XRD analysis with the 144 h annealed stack (chosen because the layer exchange is completed and does not evolve further upon annealing). The in-situ high-temperature GIXRD patterns of the 144 h annealed stack are shown in Figure 7(b). The patterns show that while the d^{hkl} of the poly-SiGe phase is almost constant, the expansions in d^{hkl} of the Al lattice at high-temperature are clearly visible as shift in d^{hkl} toward lower 2θ values. The Al peaks shift back to higher 2θ value close to the initial dhkl upon cooling to RT. The in-situ stress prevailing at high temperature was then analyzed using the multi-hkl peak shift method by plotting the ψ-dependence of Al's *a* as shown in Figure 7(c). The reversal of the thermal stress from tensile at RT to compression at high temperature, i.e., above 250 °C, is clearly observed. The compressive stress reverts back to tension upon cooling down to RT again showing that the lattice expansion in this temperature range is completely within the elastic (Hooke's) limit. This result clearly shows that the origin of layer exchange during the AIC process is the built-up of compressive stress/strain due to the nucleation and growth of poly-SiGe phase in the Al layer. Finally, the top Al layer is removed by selective etching with diluted HCl at 60 °C to leave only poly-SiGe thin film on glass. However, owing to the finite solubility of Al in SiGe at 350 °C, the resulting poly-SiGe thin film is degenerately doped with Al and is p-type.

Au-Si system

The Au-Si system has a $T_{e(Au\text{-}Si)}$ ~ 363 °C. The crystallization characteristics of a-Si in a-Si(200 nm)/Au(~ 250 nm)/glass thin film stack having no interfacial oxide layer is presented at various T_a up to ~ 363 °C. The isothermal annealing were performed in vacuum for 6 h. At T_a = 290 °C, well below the $T_{e(Au\text{-}Si)}$, the AUILE crystallization of a-Si/Au bilayer results in Au/poly-Si bilayer thereby enabling growth of poly-Si thin film on glass. The T_a was then slowly increased to approach the $T_{e(Au\text{-}Si)}$ ~ 363 °C. The upper limit of T_a up to which solid state crystallization of a-Si via diffusion assisted layer exchange of Si and Au layer still prevail was found to be ~ 330 °C. The top and bottom images of the pristine and annealed thin film stack illustrating the layer inversion of the a-Si/Au bilayer is shown in Figure 8(a). The corresponding Raman spectra acquired (with 514 nm laser source) from both the top and bottom sides (through the glass substrate) of the annealed stacks are shown in Figure 8(b). The spectrum acquired from the bottom side exhibits the well-defined characteristic Si peak at wave number ~ 521 cm^{-1}. This peak originates from the vibrational mode of Si–Si bond in the crystallized Si grains. The spectrum acquired from the top side (now occupied by Au) on the other hand does not exhibit any Si peak, thereby confirming the layer inversion process. In addition, the Raman spectrum from the pristine a-Si exhibiting a broad peak at ~ 480 cm^{-1} is also shown for reference.

As T_a increases to ~ 363 °C, the a-Si/Au bilayer on glass exhibits remarkably different crystallization behavior without exhibiting any conspicuous layer exchange. Although diffusion is still prevalent, the crystallization ceases to be a pure solid-to-solid phase transformation process due to the onset of eutectic alloying, leading to the formation of c-Si grains with different fractal patterns, as seen in the FESEM micrograph of Figure 9. Two regions with

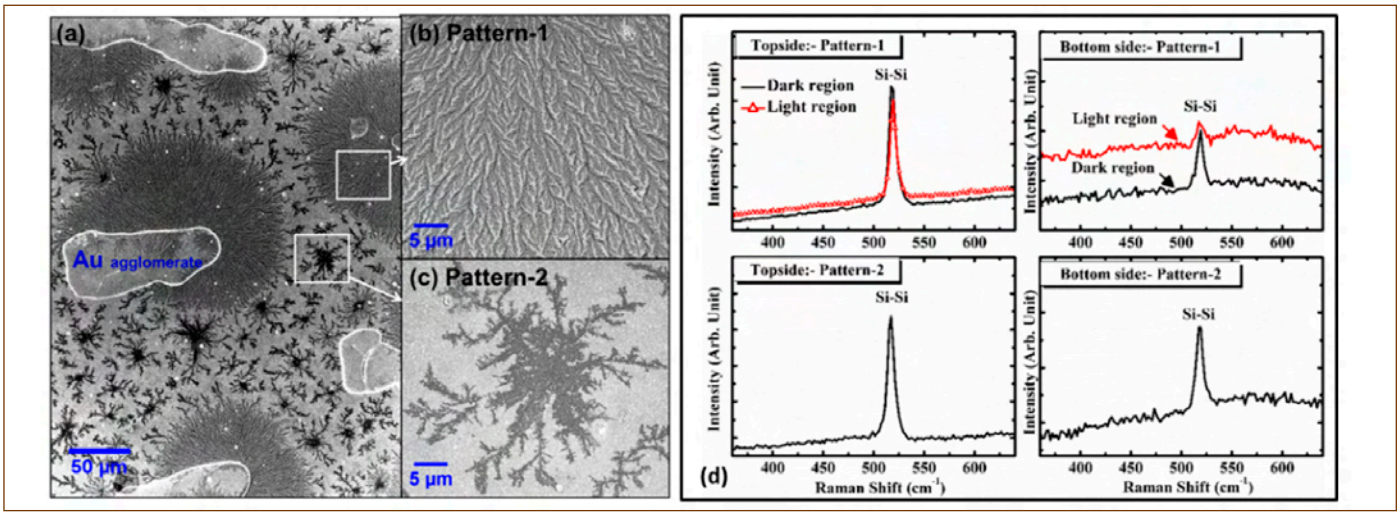

Figure 9: (a) FESEM micrographs of the a-Si/Au stack after annealing at 363 °C for 6 h showing regions with different microstructure: - (b) pattern-1 and (c) pattern-2. (d) Raman spectra from pattern-1 and 2

distinct microstructural features can be identified: - (a) Region of Interest (RoI)-1 having a fine mesh of Si grains entrained in an Au matrix (pattern-1, Figure 9(b)) and (b) RoI-2 having isolated Si grains (measuring several μm in size) growing on the glass substrate (pattern-2, Figure 9(c)). These microscopic regions have evolved due to the following competing diffusion processes: - i) the GB wetting and subsequent diffusion of Si into the Au GB and ii) the dissolution of Si into Au at the a-Si/Au interface.

The first process proceeds via the diffusion assisted solid-state Au-induced crystallization and lead to heterogeneous nucleation of c-Si at the Au GB or the glass substrate. On the other hand, the second process leads to the formation of a mixed Au-Si melt at the interface when Si concentration reaches near the eutectic composition of Au-Si alloy (i.e., $Au_{0.81}$-$Si_{0.19}$). However, not all the Au-Si goes into the liquid phase as the Si fraction in excess of eutectic composition remains in the solid phase. The supply of additional Si atom to the growing c-Si nuclei then proceeds via diffusion of Si through the melt. As a result, a non-equilibrium diffusion-limited-aggregation-like growth of c-Si ensues, resulting in the fractal pattern-2 wherein, the nuclei expand radially outward from the nucleation centers. On the other hand, fractal pattern-1 exhibits continuous inter-branching of Si and Au with no clear nucleation center. It results from the phase segregation of Si and Au from the mixed Au-Si melt upon cooling. However, the Raman spectra from the Si phase in both the RoIs exhibit the characteristic c-Si peak at $\sim$ 521 cm^{-1}, confirming the crystallinity of the Si grains as shown in Figure 9(d). Hence, the realization of a poly-Si thin film on any foreign substrates through the AUILE crystallization process is possible only if the processing temperature or T_a is less than the $T_{e(Au-Si)}$. In general, this will hold true for all the binary eutectic forming metal-Group-IV semiconductor couples.

The key findings from the studies are summarized below:

1. The crystallization temperature of amorphous Ge thin film was lowered to $\sim$ 300 °C using the catalytic Al-induced crystallization process, wherein the Al grain boundaries were found to play a vital role. The absence of grain boundaries not only retards this interface controlled crystallization, but also suppress the associated layer exchange phenomenon.

2. The use of Au further reduced the crystallization temperature of amorphous Ge to $\sim$ 170 °C. The role of interface energetics, particularly the Au's GB, in enabling the AUILE crystallization process was explained. The poly-Ge thin film exhibits p-type semiconducting behaviour due to point defects induced acceptor states. The suitability of this route for realizing poly-Ge thin film on glass and polymer substrates was demonstrated.

3. Poly-SiGe thin film was also realized on glass at 350 °C using ALILE crystallization process. The role of stress/strain in the layer exchange that occurs during ALILE crystallization was comprehensively explained. The poly-SiGe thin films act as a degenerate p-type semiconductor due to doping by Al during ALILE process.

4. Au-induced crystallization of amorphous Si thin film was performed in the temperature range 290 to 363 °C. The change in the AUILE crystallization behaviour as the Te(Au-Si) is approached was elucidated.

Young Researcher's Forum

Shri Dillip Kumar Mohapatra is working as a senior research scholar in Smart Materials Section, CSTD, MCG, MMG, IGCAR. He acquired M.Sc. in physics from Jawaharlal Nehru University, New Delhi and joined IGCAR in 2015, registered for PhD with HBNI under the guidance of Dr. John Philip. His research topic is studies on parameters influencing field induced microstructures in magnetic fluids and its influence on optical properties. He has authored 4 journal publications and is the recipient of Best Poster Award, International Conference on Nano Science and Technology (ICONSAT 2020), Kolkata, India..

Magnetic Field Tunable Structures in Dispersions Containing Superparamagnetic Nanoparticles

A ferrofluid is a stable colloidal suspension containing superparamagnetic nanoparticles dispersed in a carrier fluid. Magnetic field induced structural transitions in ferrofluids have been a topic of interest from both the fundamental and practical point of view. The self-assembly of magnetic nanoparticles under an external magnetic field gives rise to interesting optical properties. Particle-size polydispersity is inevitable in any ferrofluid, and it plays an important role in field-induced structure formation. A polydisperse fluid can be considered as a mixture of a large number of components, where the particle size, shape, or interaction strength may vary. This not only affects the equation of state for the system, but also the phase transitions. Despite the vast number of studies on the field-dependent properties of ferrofluids, most of the research until now has been confined to equilibrium or steady-state properties. In many technological applications, ferrofluids are subjected to magnetic-field but the behavior of ferrofluids depends on the properties of suspended nanoparticles. However, the exact conditions at which different structures such as thin chains, thick chains, sheets, isotropic bubbles, hexagonal and lamellar/stripe structures are largely unknown. Here, we detail the field-induced microstructures in ferrofluids with different polydispersity indices (PDIs), with either in-plane or out-of-plane fields with respect to the confining cell. Phase contrast optical microscopy, light scattering, and magnetization experiments are used to characterize the structures formed in three ferrofluids with various PDIs, and the experimental results for a high-PDI case are complemented by Brownian-dynamics simulations.

Three different ferrofluids containing oleic-acid stabilized magnetite (Fe_3O_4) nanoparticles at the same volume fraction (Φ=0.037) were used in the present study: these three samples were named M1, M2, and M3. The particles were synthesized using the co-precipitation technique, and then dispersed in kerosene as the carrier fluid. The average crystallite diameters of the particles were 9.6 nm, 8.3 nm, and 10.5 nm for samples M1, M2, and M3, respectively. To complement the experimental study, and to gain additional insights on field-induced structure formation, Brownian dynamics simulations of sample M3 were carried out. Table 1 reports the consolidated physical properties of the three samples. The polydispersity index obtained from the DLS study is defined as PDI=$(s_\sigma/\mu_\sigma)^2$ where s_σ and μ_σ are, respectively, the standard deviation and mean of the hydrodynamic diameter (σ) distribution. The amount of surfactant required to form a monolayer was computed and is compared with that of the experimental data (Table 1).

Table 1. Physical properties of the samples M1, M2, and M3.

Sample name	Crystallite diameter (nm)	Hydrodynamic diameter (nm)	Polydispersity index	Magnetization (emu/g)	Surfactant weight loss (%)	Surfactant wt% required for a monolayer
M1	9.6 ± 0.7	10 ± 0.6	0.22	69 ± 0.6	24	19
M2	8.3 ± 0.6	11.7 ± 0.9	0.23	66 ± 0.7	21	21.4
M3	10.5 ± 0.6	20.9 ± 1	0.79	71 ± 0.7	19	17.7

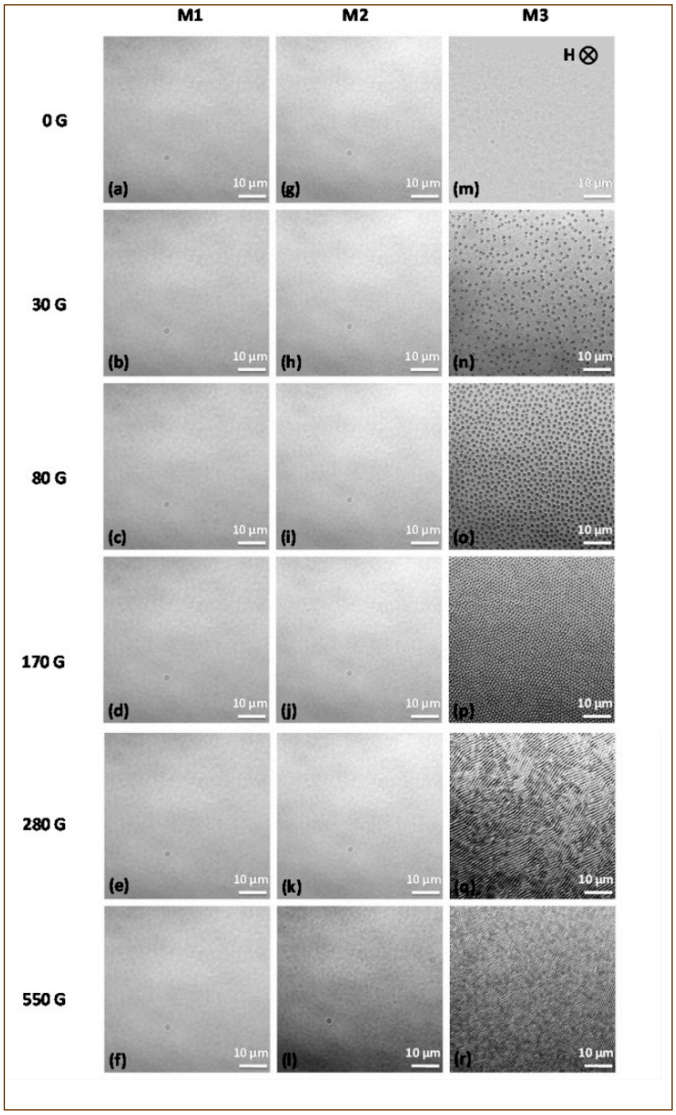

Figure 1: Phase contrast optical microscopy images showing cross-sectional views (top views) of field-induced microstructures in samples M1 (a)–(f), M2 (g)–(l), and M3 (m)–(r), at different out-of-plane magnetic field strengths of 0 G, 30 G, 80 G, 170 G, 280 G, and 550 G. The volume fraction is Φ=0.037 in all three samples, and the direction of the magnetic field H is perpendicular to the plane, as shown by an arrow in Figure 1(m)

The field-induced microstructures formed at different magnetic field strengths in samples M1, M2, and M3 sample were studied using a phase contrast optical microscope. The external magnetic field was varied by using two permanent magnets placed in the two arms of a motorized stage, where the distance between the arms was varied using a stepper motor control. The magnets were brought closer to one another at different speeds (the 'ramp rate'), giving different magnetic field strengths, and the resulting images were captured.

Cross-sectional views of magnetic field-induced microstructures in samples M1, M2, and M3 at different magnetic field strengths of 0 G, 30 G, 80 G, 170 G, 280 G, and 550 G are shown in Figure 1. Here, the external magnetic field was applied perpendicular to the sample plane (out-of-plane). Cross-sectional views of columns and sheets appear as 'bubbles' and stripes, respectively. No bubbles are observed in sample M1 at any magnetic field strength up to 550 G, which indicates that any aggregates are less than 100 nm in size. In sample M2, only a few bubbles are seen at the highest field strengths of 280 G and 550 G.

Although the polydispersity is very high in sample M3, in zero field, all particles are well dispersed in the sample, and even if there are aggregates of larger particles, their size is much less than the 100 nm resolution limit of the microscope. Hence, no structures are observed in the absence of a magnetic field, but bubbles appear even at the very low magnetic field strength of 30 G. In this case, the bubbles are randomly positioned in the plane, with an average intercolumn spacing of 3 μm. There are more columns at a field strength of 80 G, with a smaller intercolumn spacing of 1.5 μm. Hexagonal close packed columnar structures are apparent above a magnetic field strength of H=170 G, with an even smaller intercolumn spacing of 0.6 μm. Overall, the average intercolumn spacing is found to vary inversely with the external magnetic field strength (αH^{-1} with $R^2 \simeq 0.99$) up to a field strength of 170 G, beyond which the columns coalesce and form stripe patterns. At a field strength of 280 G, columns coalesce through lateral interactions to form stripe patterns (lamellar structures), with the stripes being extended perpendicular to the direction of the external magnetic field. The average width of a stripe at 280 G is 1.6 μm. As the field is increased further to 550 G, the number of stripes increases, the thickness of the stripes decreases, and the distance between the stripes decreases to 0.7 μm. At 280 G, the stripes are parallel to each other without significant bending. At 550 G, however, the stripes show a zig-zag modulation. This instability or undulation at 550 G can be understood as follows. As the field is increased, the width of the stripes decreases, while the length of the stripes increases (Figure 1). In addition, since the ferrofluid is a paramagnetic substance, the local concentration of magnetic material in the cell volume should increase with increasing field strength, with particles being supplied by the surrounding ferrofluid reservoir. Since the stripe structures are confined in the field direction (the cell thickness was approximately 21 μm), the simplest way to increase the length is through undulation. The zig-zag pattern gives rise to a larger area of interaction between the stripes, which leads to stabilization through the long-range magnetic interaction between stripes.

To sum up, in sample M3, three different structural arrangements of columns occurred in the presence of an out-of-plane field, these being isotropic, hexagonal, and stripe/lamellar structures with increasing magnetic field. These structures are shown in more detail in Figure 2.

Figure 2(a)–(c) shows the structural progression between

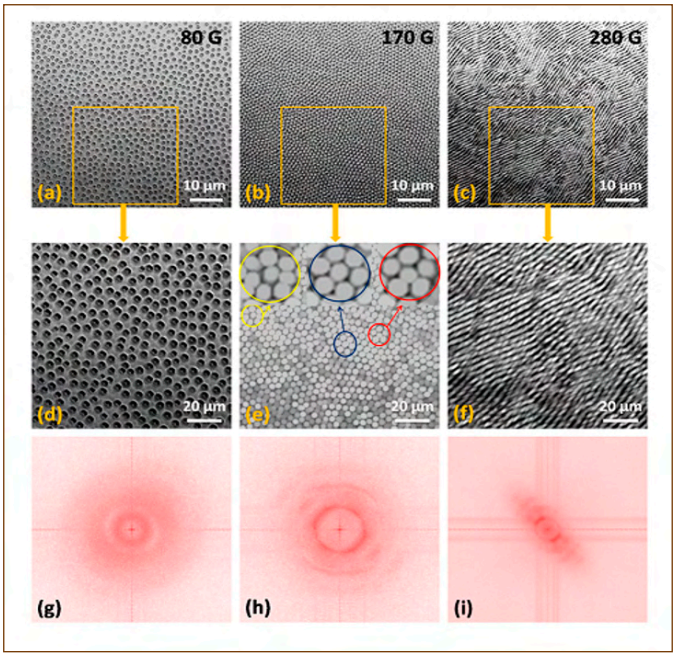

Figure 2: (a)–(c) Phase contrast optical microscopy images of sample M3 showing the isotropic, hexagonal, and stripe/lamellar phases with out-of-plane magnetic field strengths of 80 G, 170 G, and 280 G, respectively. (d)–(f) Enlarged views of the images in (a)–(c). (g)–(i) FFT images of selected areas from (d)–(f).

isotropic, hexagonal, and stripe patterns in sample M3 with magnetic field strengths of 80 G, 170 G, and 280 G. Figure 2(d)–(f) shows enlarged views, and Figure 2(g)–(i) shows corresponding fast Fourier transform (FFT) images of the isotropic columnar distribution, hexagonal arrangement of columns, and stripe patterns. At H=80 G, all columns are distributed randomly, and hence the FFT gives a circular pattern as shown in Figure 2(g). At H=170 G, the columns are closer to one another, and adopt local 2D hexagonal coordination but without long-range order. Close inspection of the FFT patterns reveals that the enlarged image [Figure 2(e)] contains both five-fold and seven-fold coordination sites, along with the expected six-fold coordination sites. Five-fold and seven-fold coordination sites coincide with the positions of bubbles that are, respectively, smaller and larger than the bubbles that surround the six-fold coordination sites. It is known that size polydispersity creates dislocations and bubble-area mismatches, leading to size adjustment of the five-fold and seven-fold coordinated bubbles. Due to the misorientation of columns, a hexagonal pattern is seen in Figure 2(h), instead of the six diffraction spots expected for a perfect hexagonal structure. Similar hexagonal patterns have also been seen in other systems such as a charged superparamagnetic colloid of $Fe3O_4$ nanoparticles coated with silica, and a ferrofluid with magnetic holes (nonmagnetic particles dispersed in a magnetized ferrofluid solution). The stripe pattern [Figure 2(i)] indicates periodic ordering of the domains along the longitudinal direction of the pattern, and the angular distribution indicates the directionality of the stripe pattern. When stripes are parallel to each other, two spots are seen in Figure 2(i). The increased magnetic moment and decreased column separation at 280 G cause a stronger repulsion between the columns, which results in the aggregation of columns into lamellar structures in order to minimize the free energy.

The scattered light intensity pattern from samples M1, M2, and M3 at magnetic field strengths of 0 G, 80 G, 170 G, and 550 G are shown in Figure 3. In the absence of a magnetic field, there is no clustering of the magnetic nanoparticles, and since the particles are smaller than the wavelength of incident light ($\sigma << \lambda$), Rayleigh scattering gives rise to one central spot on the screen. When the size of the scatterers is comparable to the wavelength of incident light, the scattering changes from the Rayleigh to the Mie regime. In case of sample M1, the spot intensity remains unchanged with an increase of the magnetic field strength, indicating that the scatterer size remains within the Rayleigh regime. Due to the presence of only smaller aggregates such as pairs, triplets, and other small chains, no changes in the intensity of the transmitted light spot are observed. In sample M2, there is a slight decrease in light intensity at 80 G. At 170 G, intense speckles of white spots and dark spots appear around the central spot. The speckle pattern formed when light passes though the magnetic nanofluid is due to the interference of dephased scattered waves emanating from randomly positioned particles. The structural transition from disorder to order in colloidal media has been studied by measuring such speckle parameters. The scattered waves from ordered media remain in phase rather than be dephased, which increases the probability of constructive interference of scattered wave. As the field increases, the number of single chains increases in the direction of the magnetic field. At 550 G, the system contains isolated particles, pairs, triplets, small chains, and large chains. The number of speckles and the speckle contrast both increase, and the speckles are arranged in a circle indicating that linear aggregates are formed along the light-propagation direction. The increase in speckle contrast indicates a decrease in the mobility of the growing aggregates on increasing the magnetic field strength.

In sample M3, the transmitted light spot at zero field is transformed into a circular pattern at 80 G, where the speckles are distributed on the circumference of circle, indicating the formation of long chains and zippered columns that are distributed randomly in the sample. The reason for the formation of a circular pattern can be explained on the basis of light scattered by cylindrical surfaces. On placing a screen at some distance from the cylinder (parallel to the incident light) the scattering pattern forms a conic section. For $\zeta=0°$, the scattered pattern will be a circle as shown for sample M3 at 80 G in Figure 3(j), where ζ is the angle between the incident light wave and the cylindrical axis. The scattered pattern

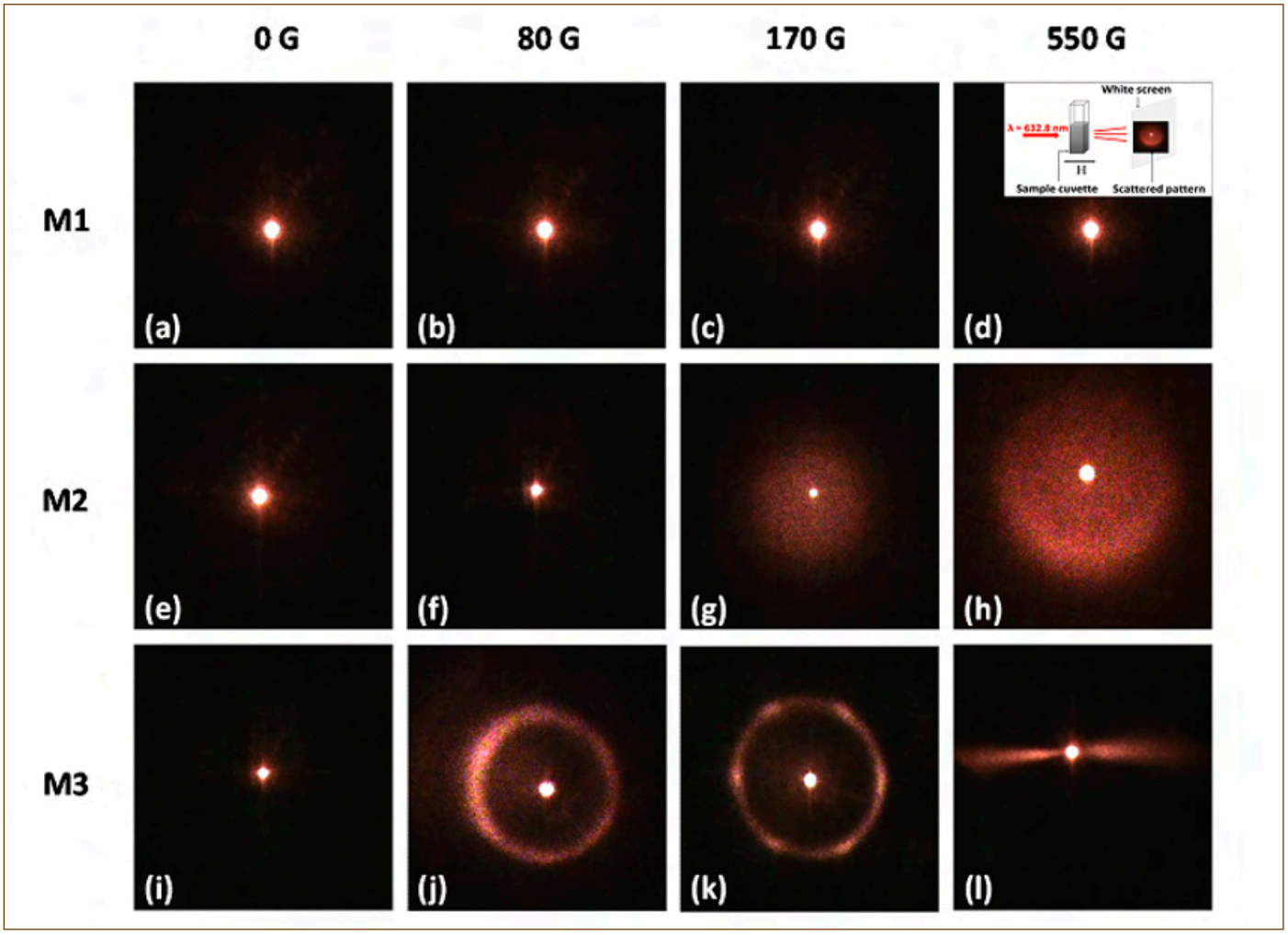

Figure 3: Scattered light intensity pattern from samples M1, M2, and M3 at magnetic field strengths of 0 G (a, e, i), 80 G (b, f, j), 170 G (c, g, k), and 550 G (d, h, l). The inset of Figure 3(d) shows the schematic representation of light scattering measurement

forms an ellipse at $0°<\zeta\leq45°$, and transforms into a hyperbola at $45°\leq\zeta\leq90°$. When the incident light is normal to the cylinder axis, a straight-line pattern is formed. In sample M3 at 170 G, six bright spots with some speckles are observed at the circumference of the circular pattern, indicating the presence of a short-range ordered hexagonal pattern. At 550 G, a straight-line pattern is observed due to the scattering of light from stripe-like structures, which is analogous to the scattering pattern form a straight line when the incident-light direction is normal to the cylinder axis.

Brownian dynamics simulations are used to gain further insight on the crossover between columnar and stripe patterns in sample M3. Figure 4 shows top-down views of systems corresponding to H=280 G, and Φ=0.037 and 0.222. For each system, an orthographic view and a perspective view are shown, so that the presence of chains in the field direction can be discerned. In the case of the orthographic view, four periodic replicas are shown in the xy plane, so that any clusters cut by the box edge can be distinguished. At Φ=0.037, it is clear that long chains of large particles have formed in the field direction, but many of the small particles are not part of any cluster. Some chains are one-particle thick, and others are zippered. The orthographic view – where the particle positions are projected on the plane – shows some clustering, but the distinction between clusters and free particles is not very clear. Increasing the volume fraction does not produce any interesting structure. As shown in Figure 4, at Φ=0.222, no distinct clusters can be identified clearly from either view.

Higher field strengths are required to produce more distinct clusters. Figure 5 shows snapshots from simulations at a field of 415 G (halfway between the experimental values of 280 G and 550 G), and at six volume fractions in the range Φ=0.037-

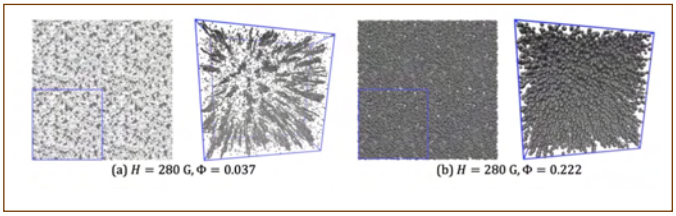

Figure 4: Snapshots from simulations with H=280 G and (a) Φ=0.037, and (b) Φ=0.222. In each case, an orthographic view (with 4 periodic replicas) and a perspective view are shown.

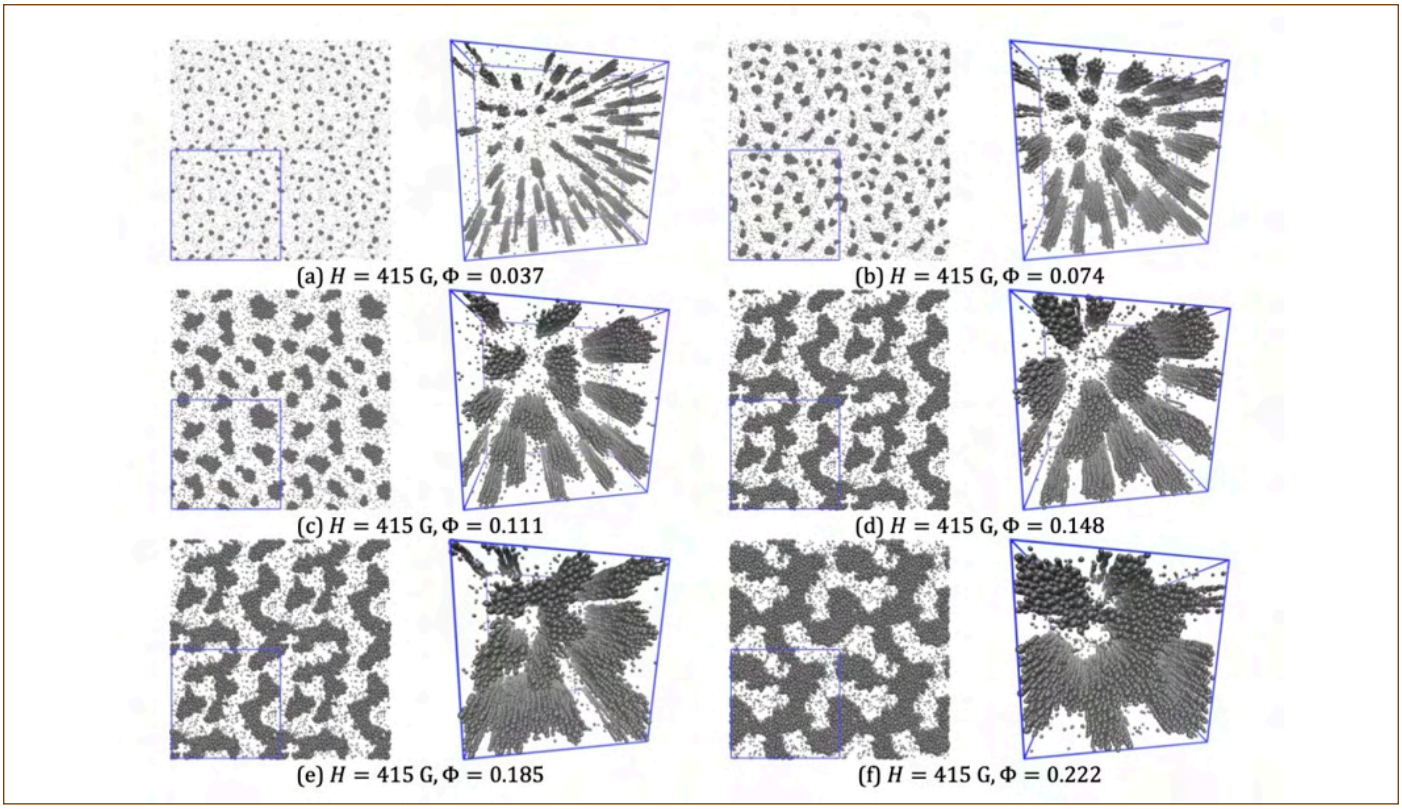

Figure 5: Snapshots from simulations with H=415 G and (a) Φ=0.037, (b) Φ=0.074, (c) Φ=0.111, (d) Φ=0.148, (e) Φ=0.185, and (f) Φ=0.222. In each case, an orthographic view (with 4 periodic replicas) and a perspective view are shown.

0.222. The results are dramatically different from those at the lower magnetic field strength. Firstly, a much greater proportion of particles are now associated with columns, meaning that the clusters are much more distinct in the snapshots. At the three lowest volume fractions (Φ=0.037, 0.074, and 0.111), the columns mostly have cylindrical symmetry, and are evenly spaced in the xy plane, but without long-range ordering. At higher volume fractions (Φ≥0.148) the columns have coalesced to form structures that are more extended in the direction perpendicular to the field, and as the volume fraction is increased, they begin to connect up further to form something resembling a continuous, labyrinthine structure. The perspective views clearly show the sheet-like structures formed by the coalescence of the columns.

The effect of size polydispersity on field-induced equilibrium and non-equilibrium structures in magnetic nanofluids was probed systematically. Three different ferrofluids – labelled M1, M2, and M3 – containing magnetic nanoparticles with average crystallite diameters 9.6 nm, 8.3 nm, and 10.5 nm, and with different polydispersities, respectively, were studied. Phase contrast optical microscopy images revealed that sample M3 showed structural transitions from isotropic columnar, through hexagonal close packed, to striped patterns on increasing the magnetic field between 0 G and 500 G. In contrast, samples M1 and M2 showed no such structural transitions.

In summary, the influence of particle size polydispersity on field-induced structures and structural transitions in magnetic fluids (ferrofluids) is studied using phase contrast optical microscopy, light scattering and Brownian dynamics simulations. Three different ferrofluids containing superparamagnetic nanoparticles of different polydispersity indices (PDI) are used. In a ferrofluid with high PDI (~0.79), thin chains, thick chains, and sheets are formed on increasing the in-plane magnetic field, whereas isotropic bubbles, and hexagonal and lamellar/stripe structures are formed on increasing an out-of-plane magnetic field over the same range. On the contrary, no field-induced aggregates are seen in the sample with low polydispersity under the above condition. In polydisperse sample, bubbles are formed at a very low magnetic field strength of 30 G. Insights into the structural evolution with increasing magnetic field strength are obtained by carrying out Brownian dynamics simulations. The crossovers from isotropic, through hexagonal columnar, to lamellar/stripe structures observed with increasing field strength in the high-polydispersity sample indicate the prominent roles of large, more strongly interacting particles in structural transitions in ferrofluids. Our work opens up new opportunities to develop optical devices and accessing diverse structures by tuning size polydispersity.

Events

- Hindi Fortnight Prize Distribution Function, Hindi Section, February 4, 2021
- Workshop on Scientific Writing for Journals by Ms. Swati Meherishi, Editorial Director, Applied Sciences, Springer Nature, SIRD, February 18, 2021
- Theme meeting on Innovative I&C concepts & Technologies for Nuclear Reactor (I2CT-21), EIG, February 24-25, 2021
- Closing Ceremony of Swatchhta Pakhwada at Raja Ramanna Auditorium, February 26, 2021
- Lecture on Parenting, IWSA, March 17, 2021
- Awareness of Laws & Accessibility of the Courts to Women in India By Smt. Adhilakshmi Logamurthy, Advocate, High Court, Chennai, IWSA, March 22, 2021

HBNI-IGCAR CI

Ph.D Thesis Defense

Name	Title	Date	Discipline
Shri. Shubhra Sarkar	N-H—X (X=O, N, π) Hydorgen bonded interactions of Pyrrole: Matrix Isolation Infrared and Computational Studies	15/03/2021	Chemical Sciences
Shri Gopinath Sahoo	Surface Modication and Polymer-Free Transfer of Vertical Graphene Nanosheets for Electrochemical Capacitor Applications	21/01/2021	Physical Sciences
Shri P. T. Rakesh	Observational Analysis and Numerical Simulation of Meteorological Phenomena Leading to Severe Radiological Impact	15/03/2021	Physical Sciences

Awards, Honours and Recognitions

Smt. S. Rajeswari, SIRD, Winner, Real Impact Awards 2020 : Library Commitment to Impact, by Ms Emerald Publishing, UK.

Ms.T. P. Rasitha, SRF, CSTD, MMG has been awarded "NACE Foundation India Scholarship" of Rs.1,50,000/- by the NACE Foundation (USA)

Best Paper/Poster Awards

Best Paper Award

S. C. S. P. Kumar Krovvidi, J. Veerababu, Sunil Goyal, A.Nagesha, A. K. Bhaduri
Viscoplastic Constitutive Parameters for Inconel Alloy-625 at 843K
Structural Integrity conference and exhibition (SICE-2020), IIT-Mumbai, December 2020

S. C. Vanithakumari, R. P. George, John Philip
Development of Superhydrophobic Coating on Steel by Electrospinning
National Symposium on Electrochemical Science and Technology 2020(NSEST-2020) held via online mode, Bengaluru, January 21-22, 2021

Bio-diversity @ DAE Campus, Kalpakkam

Asian Paradise-Flycatcher is an insectivorous bird with small flat bill and bristles at the gape which help in the capture of flying insects. The wings and the tail are mostly chestnut colored and the plumage below is grayish white. The crown and crest are glossy black. It has two long narrow ribbons like tail feathers. Males have streamers in tail and blue eye rings.

Published by Scientific Information Resource Division, SQ&RMG, IGCAR, Kalpakkam-603102